RIGID & ELASTIC COMPOSITE REGISTRATION OF 3D LEG T1-WEIGHTED MR IMAGES FOR STRAIN ANALYSIS

by

Ekberjan Derman

B.S., Optical Communication Technology, South China University of Technology, 2009

Submitted to the Institute for Graduate Studies in
Science and Engineering in partial fulfillment of
the requirements for the degree of
Master of Science

Graduate Program in Electrical and Electronics Engineering
Boğaziçi University

2013

ACKNOWLEDGEMENTS

This work has been supported by the Scientific and Technological Research Council of Turkey (TÜBITAK), with project number: 111E084, the project manager is Assoc. Prof. Can. A. Yücesoy, from biomedical engineering department of Bogaziçi university.

The author would like to thank Alper Yaman, a PhD student from biomedical engineering department of Bogaziçi university, and Serkan Çimen, a former Vavlab member of department of EE, Bogaziçi university, for their useful help and discussion.

ABSTRACT

RIGID & ELASTIC COMPOSITE REGISTRATION OF 3D LEG T1-WEIGHTED MR IMAGES FOR STRAIN ANALYSIS

Strain analysis of deformation field is a crucial step for scientific analysis of muscle structures in MRI data sets. They are commonly used for different types of data analysis such as force transmission among muscles which is one of the popular topics in recent years. Especially there is a popular trend of research concentrating on force transmission among lower leg. For successfully carrying out these types of tasks, a correct and effective deformation field of the MRI data must be obtained in order to get the expected corresponding strain assessments. These deformation fields are usually obtained by registration framework, in which two groups of data sets were registered to one another, one serving as moving data set, which is transformed to the other target, static data set. Formerly, in registration framework, the whole region of MRI, including bones, is elastically registered to each other. However, bone tissues are relatively hard comparing to those soft muscles, elastically registering these hard tissues, which yields non-zero deformation values among these regions, could negatively affect the correctness of the obtained final result. For that, we can think of keeping these bone regions as fixed, and then elastically register the remaining parts to obtain a deformation field in which there would be zero deformations in the bone regions. In this work, T1-weighted MR images of lower leg of human body in undeformed and deformed states are selected as test data. We first segment the bone regions, keep them as fixed, then perform elastic registration on the remaining parts on MR images of lower legs, and compare the obtained strain analysis of deformation field results with those from unconstrained elastic registration method. We expect to see the final result would be better than the one obtained by unconstrained elastic registration.

ÖZET

GERİLİM ANALİZİ İÇİN 3B BACAK T1-AĞIRLIKLI MR GÖRÜNTÜLERİNİN KATI VE ELASTİK BİLEŞİK ÇAKIŞTIRILMASI

Deformasyon alanının gerilim analizi MRG veri setinde kas yapılarının bilimsel analizi için kritik bir adımdır. Onlar son zamanlarda popüler konulardan biri olan kas kuvvet iletimi gibi çeşitli veri analizleri için kullanılmaktadır. Özellikle, alt bacakta kas kuvvetinin iletimine yoğunlaşan popüler araştırma eğilimi oluşmuştur, ve bu tür araştırmalarda gereken MRG verilerin gerilim analizi kullanılmaktadır. Bu tür araştırmaların başarısı için doğru ve etkin deformasyon alanının elde edilmesi gerekiyor. Bu deformasyon alanları genelde çakıştırma yöntemiyle elde ediliyor. Çakıştırmada iki grup veri setlerin birinin hareket eden set olarak diğer sabit setle çakıştırılıyor. Önceki çakıştırma yöntemlerde kemiği içeren tüm MRG alanı bir biriyle çakıştırılmıştı. Ama, kemik dokularının kas dokularına göre sert olduğunu düşünürsek, bu sert kemik dokularının elastik olarak çakıştırılıp kemik bölgelerinde sıfır olmayan deformasyon verileri vermesi elde edilen deformasyon sonucunu negatif etkilemiş olabilir. O nedenle, biz kemikleri sabitleyerek diğer bölgeleri elastik çakıştırmayı, ve böylece kemik bölgelerinde sıfır deformasyon almayı düşüne biliriz. Bu çalışmıda, insan alt bacağın T1-ağırlıklı deforme oluşmuş ve oluşmamış haldeki MRG veri setleri kullanılmıştır. Biz önce kemik bölgeleri segmentasyon takiben sabit tutarak, diğer bölgeleri elastik şekilde çakıştırıyoruz, ve deformasyon sonucunu öncekiler kullanan tüm elastik çakıştırma metodunun sonucu ile karşılaştırıyoruz.

TABLE OF CONTENTS

LIST OF FIGURES

LIST OF TABLES

LIST OF SYMBOLS

D_i	Initial vector space built by $P_{R'}$
D_{final}	Final deformation field obtained by rigid+elastic registration
$I_{F(X)}$	Fixed original image
$I_{M(X)}$	Moving original image
$I_{M(X)'}$	Transformed moving image obtained by transforming the original moving image with P_R
P_R	Parameters obtained by rigid registration of $\varphi_{M(X)}$ and $\varphi_{F(X)}$
$P_{R'}$	Registration parameters obtained by rigid registration of $\chi_{M(X)'}$ and $\chi_{M(X)}$
T	Coordinate transformation
$\varphi_{F(X)}$	Segmented tibia mask of original fixed image
$\varphi_{M(X)}$	Segmented tibia mask of original moving image
$\varphi_{M(X)'}$	Segmented tibia mask of $I_{M(X)'}$
$\chi_{F(X)}$	Segmented fibula mask of original fixed image
$\chi_{M(X)}$	Segmented fibula mask of original moving image
$\chi_{M(X)'}$	Segmented fibula mask of $I_{M(X)'}$

1. INTRODUCTION

The fundamental requirement to move the limbs in order to accomplish several tasks is the exertion of force onto the bony skeleton. Muscle is the motor for generation of the necessary force. The exertion of force involves not only generation, but also transmission of it. According to the common view, due to its highly specialized morphology, the myotendinous junction, which is the junction between the ends of muscle fibers and the aponeurosis, has been very widely regarded as the exclusive site for transmission of force from muscle fibers where the force is generated. According to this point of view, commonly the individual skeletal muscles are considered as independent functional units which have unique muscle length-force characteristics [1].

Muscle fibers and intramuscular connective tissue stroma are, however, connected to each other along the full periphery of muscle fibers, in addition to the myotendinous junctions. Such connection is provided by complex supramolecular structures: the cytoskeleton is connected to laminin, by trans-sarcolemmal molecules, which is connected to the basal lamina, which in turn is connected to the endomysium that is responsible for forming a 3D structure of tunnels within which the muscle fibers are operating [2].

Recently, it has been speculated that the transmission of muscle force is not limited to the myotendinous junction exclusively, but also involves a complex network of pathways provided by the myofascial apparatus [1]. Myofascial force transmission occurs between muscles (intermuscular myofascial force transmission) and from muscles to the surrounding nonmuscular structures such as neurovascular tracts and bone (extramuscular myofascial force transmission) [3]. The main reason behind this new view is the fact that muscle fibers and the extracellular matrix are connected not only at the myotendinous junctions, but also along the remainder of the full perimeter surface of the muscle fibers, which plays a significant role in force transmission shown by experiments. At the same time, neighboring muscles are connected not only to each other but also to the boundaries of the compartments within which they operate.

The significance of this new view is that, if force is transmitted not only between muscles but also from muscles to nonmuscular structures via myofascial pathways, it is inappropriate to regard individual muscles as fully independent functional units anymore. Further, the parameters of muscle length-force characteristics, such as muscle optimum length and optimal force, are not specific properties of individual muscles, due to the integrated effects of intra- inter- and extramuscular myofascial force transmission. Instead, the relative position of muscle with respect to its neighboring muscles and nonmuscular connective tissue structures also affects the actual muscle length-force characteristics. Thus, rather than individual muscles, groups of neighboring synergistic muscles may form functional units [1]. Some potential fields that can be impacted by this novel view of myofascial force transmission include motor control in nervous system, including sensory information and coordination of different muscles, and muscle diseases such as diseases associated with over-use, and genetic muscle diseases. There is evidence that epimuscular myofascial force transmission is related to the basic muscle mechanics, and the etiology of diseases, that can lead to better the therapeutic methods [4].

This hypothesis was studied quantitatively and tested using a combined finite element modeling and experimental approach, concluding that individual muscles should not be viewed as fully independent functional units if force is transmitted between the muscles as well as from the muscles to the nonmuscular structures via myofasical pathways [1]. Also, this kind of force transmission was shown in animals for whole lower leg and antagonistic muscles [2]. Yucesoy *et al.* [3] tested the hypothesis that due to inter-antagonistic epimuscular myofascial force tranmission, length changes of deep flexors affect substantially the mechanics of anterior crural and peroneal muscles, and concluded that such force transmission occurs within the entire lower leg of the rat. Recently using MRI, this type of force transmission has also been confirmed for human muscles *in vivo* [5].

All of these studies testing the myofascial force transmission include strain analysis of the deformation field obtained by registering different MRI datasets acquired with different leg positions. Thus, for successfully carrying out these types of tests, it is

necessary to obtain an accurate deformation field via registering the MRI datasets. The deformation fields in these experiments were obtained by registering the test datasets in elastic mode, in which the bone regions are also registered elastically with each other.

Considering the fact that bone tissues are rigid, unlike the muscles, a non-zero deformation value in the bone region obtained by elastic registration is incorrect. Including the bone regions in the elastic registration process could have negatively affected the final deformation field obtained. Thus, a different approach should be used that keeps the bone regions rigid.

S.Steger et al. [6] recently presented a fully automated registration method based on multi-rigid registration of the skeleton for 3D images of the head and neck datasets. In their method, they first segmented the skull, the mandible and the vertebrae. Then they rigidly registered these bones with the moving image, resulting in a rigid transformation for each of the bones. Linear combinations of those transformations described the soft tissue deformation.

In this thesis, we present a new method to keep the bone regions rigid while elastically registering the remaining parts in human lower leg in 3D MR images. There are two bones in human lower leg, namely tibia and fibula. In the proposed method, we rigidly aligned the tibia, built an initial deformation field using the fibula, used it to perform constrained elastic registration to obtain the final deformation field. This obtained deformation field is then used for strain analysis. We also compared the performance of our newly proposed constrained elastic registration method with the commonly used fully elastic registration.

The significance of our proposed method is that the bone regions are no longer considered as soft, therefore there is no deformation in the bone regions. The final deformation field is more realistic, leading to an anatomically more correct strain values for analyzing the muscle force transmission.

Two sets of T1-weighted MRI data of human lower leg are acquired in load and relaxation modes. Tibia and fibula are segmented independently. Then a composite rigid and elastic registration is applied to register the two datasets such that tibia undergoes totally rigid transformation while fibula is initially registered via a rigid transform. Elastic registration is performed on the whole volume except tibia. Since the volume of fibula is much smaller than that of tibia, the elastic registration does not have a significant effect on the rigid transformation parameters initially computed for fibula. Hence, in effect, the tibia and fibula are rigidly registered while the soft tissue is elastically registered. The final registration vector field is used for strain analysis and compared to the strain analysis results obtained by full elastic registration.

The overall structure of this thesis is as follows: Chapter 2 briefly introduces the relevant background of 3D bone segmentation and registration on MRI. The full method including the 3D bone segmentation in MRI, the joint rigid and elastic registration is presented in Chapter 3. Strain analysis experiments are presented in Chapter 4, followed by a discussion and conclusion in Chapters 5 and 6 respectively.

2. BACKGROUND

2.1. Bone Segmentation in T1-weighted MR Images

In image analysis, segmentation corresponds to the process in which the object of interest is isolated from the background. The ultimate goal of segmentation is to identify the part of the data array that makes up an object in the real world. Bone segmentation in magnetic resonance imaging (MRI) has become an important task for medical diagnosis and treatment in recent years.

In this work, our test datasets are T1-weighted MR images. In T1-weighted MRI, muscle appears darker while bone appears brighter. The following figure is a typical T1-weighted MR image:

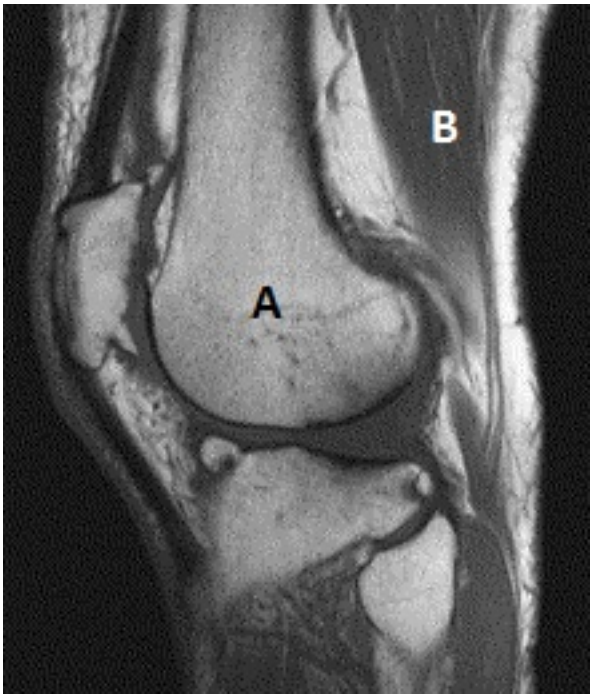

Figure 2.1. Illustration of T1-weighted bone MRI. As marked, region "A" represents bone while region 'B' represents muscle (from [7]).

In recent years particulary, the deformable models increasingly attract interest for carrying out MRI segmentation task. J. Kratky, etc [8] developed a method for

MRI bone segmentation based on a fast level set algorithm, which works in the discrete domain, and avoids solving the PDE (Partial Differential Equation) that describes the evolution of the level set. J. Schmid et al. [9] proposed a multi-resolution statistical shape model algorithm with an adapted initialization to address the bone segmentation in MR images acquired in small field of view. They presented an efficient initialization of deformable models for the hip joint MRIs. P.Dodin et al. [10] presented a fully automated segmentation method based on the ray casting technique for human knee 3D MRI bones. Their method utilizes the ray casting technique in which the MR images are decomposed into multiple surface layers obtained by a Laplacian operator in order to localize the boundaries of the bones and the final complete segmentation of the bones are obtained by automatically merging several partially segmented objects.

LM. Lorigo et al. [11] presented an automatic 2D segmentation method using texture-based geodesic active contours for the tibia and femur structures in clinical MR images of knees. In their method, input must be a small patch that is known to be within the desired structure but does not need to be anywhere near the true boundary; the active contour model flows outward from this patch until convergence. M. Koch, et al. [12] proposed a fully automatic machine learning approach for segmentation of wrist bones. Their method works in two steps: first find a bounding box around every bone, and second outlines the contour and computes a 3-D model of every carpal.

L. Shan, et al. [13] introduced a two-step process of automatic bone segmentation from MR knee images, followed by elastic tissue deformation. Their approach makes use of a fully-automatic segmentation of femur and tibia from T1 and T2 weighted MR images. A continuous convex optimization problem is the basis for their segmentation algorithm, incorporating regional and shape information. From a probabilistic viewpoint the regional terms are included, which readily allows the inclusion of shape information. The outer boundary segmentation of the cortical bone is encouraged by adding simple appearance-based information to the optimization problem. The same authors have also proposed an automatic three-label bone segmentation approach to knee segmentation (femur and tibia) from T1 and T2 MR images [14]. Unlike the binary segmentation, the separation of bones, even if they touch, has been guaranteed by

the three-label segmentation approach. They formulated the segmentation as a convex optimization problem in four dimensions assuring (given an aligned shape model) a globally optimal solution. They also further discussed a method to integrate simple appearance information to allow for segmentations of the outside of the cortical bone in MR images.

J. Schmid, et al. [15] presented automatic segmentation method of bone in low resolution clinical MRI datasets based on deformable models and shape priors. They successfully combined physical deformable models with shape priors. Models evolve under the influence of forces that exploit image information and prior knowledge on shape variations. A Principle Component Analysis (PCA) of global shape variations, as well as a Markov Random Field (MRF) of local deformations are defined by the prior, imposing spatial restrictions in shapes evolution. They also considered various levels of details and solved the system of differential equations by a fast implicit integration scheme.

J. Liu, et al. [16] proposed a rigid model-based 3D segmentation of the bones of joints in MR and CT images for motion analysis. Their method is based on a two-step model-based segmentation strategy, which utilizes the unique context of the current application in which the shape of each individual bone is preserved in all scans of a particular joint while the spatial arrangement of the bones alters significantly among bones and scans. In their first step, they generated a rigid deterministic model of the bone from a segmented bone in the image corresponding to one position of the joint by using the live wire method. Then in their second step, this model is used to seek, under rigid transformations, a segmentation of the same bones in scenes corresponding to subsequent positions of the joint.

J. Zhang, et al. [17] proposed another automatic bone segmentation method using 3D adaptive thresholding. In their method, they first performed an initial segmentation to partition the image into bone and non-bone classes, followed by an iterative process of 3D correlation to update voxel classification. The iterative process stops when no category is updated in the entire volume. The introduction of an iterative process into

the thresholding method is different from other existing 2D segmentation methods or other local adaptive thresholding methods. In their approach, only the boundary voxels are updated based on its gray value difference within the neighborhood window. They also introduced a post-processing step of 3D region growing to extract the required bone region.

H. Rifai et al. [18] addressed the segmentation of the skull in MRI using deformable models. Their method takes into account the partial volume effects that occur with MRI data. At each iteration of the propagation of the model, partial volume is estimated in a narrow band around the deformable model. They used a region-growing method to construct a preliminary segmentation of the skull, and used it as a pre-segmentation stage. An automatic 3D initialization of the deformable model has been offered by the surface that bounds the pre-segmented skull region. By using the level set method, this surface is then propagated (in 3D) in the direction of its normal, thus permitting topology changes of the surface as it evolves. The propagation speed of the model is a function of partial volume of bone.

To sum up, the MRI bone segmentation approach is increasingly used in medical related works focusing on bone regions, from wrists, to knees and skulls. As such, the MRI bone segmentation methods are continuously gaining robustness.

2.2. Registration

Image registration is the process of determining the spatial transform that maps points from one image to homologous points on an object in the second image. Image registration is a crucial step in imaging problems where the valuable information is contained in more than one image. The scope of image registration includes the following problem: given two images (or volumes), find a geometric transformation that maps the first image into the second one, which often occurs in biomedical applications. Image registration can be divided into two categories: intermodel (monomodel) registration and intramodel (multimodel) registration. Intermodel registration refers to the process when the difference between two images is only the condition of the subject,

while intramodal registration indicates the subject is imaged in essentially two different ways [19].

Image registration consists of two images, the moving image I_M and the fixed image I_F. During the registration process, the moving image I_M is deformed to fit to the fixed image I_F. Thus, registration can be regarded as the problem of finding a coordinate transformation T that makes I_M spatially aligned with I_F. The quality of the alignment is assessed by a cost function C(T;I_F,I_M). Therefore, the optimal coordinate transformation is obtained by minimizing this cost function with respect to T [20]. According to the transformation type, registration can be divided into rigid and elastic registration.

In rigid registration, the transformation is "rigid", that is, the distances between all points in the transformation remain constant. On the other hand, the elastic registration employs a transformation in which the distances between all points are no longer constant, and thus, the transformation can be very complex.

The difference in cost functions result in difference in registration methods. Mostly, these registration methods are either feature-based or intensity-based ones. The feature-based methods find correspondence between image features such as points, lines, and contours, while the intensity-based methods compare intensity patterns in images via correlation metrics. Commonly existing feature-based cost functions may include Gabor wavelets, Harris detector, SUSAN function, and Gaussian curvature based methods, while intensity-based cost functions may include the mean squared difference (MSD), the normalized correlation (NC), the mutual information (MI), and the normalized mutual information (NMI).

For carrying out the constrained elastic registration task in our work, we employed the Demons deformable registration method [21], which is one of the most frequently used methods. In physics, Maxwell's demons were introduced to model the paradoxical idea that a semi-permeable membrane could violate the second law of thermodynamics (about entropy). Situated in the membrane, those demons are supposed to sort locally

two different types of molecules of a mixed gas, to put one type on one side and the other type on the other side of the membrane, hence giving a decrease in entropy. As each demon needs to consume some energy to sort, the global entropy of the system is still increased, which suppresses the paradox.

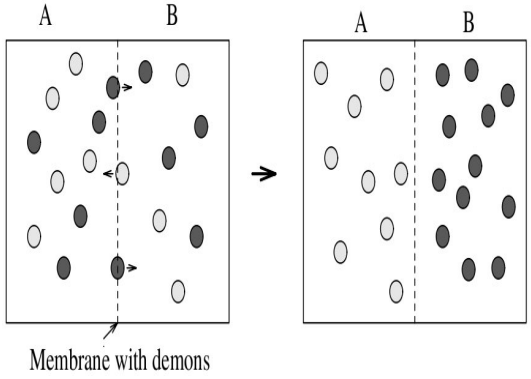

Figure 2.2. Maxwell's demons and a mixed gas (figure from [21]).

J.P Thirion [21, 22] proposed a method to perform non-rigid automatic matching of two 3D medical images based on Maxwell's demons, which locally deform the model to push it into a mold. A demon is associated with each of those contour points, in a sense very similar to Maxwell's demons. Each demon acts locally, to push the deformable model in the normal direction of the scene contour, but the orientation of the push depends on the nature (inside or outside) of the current estimate of the model at that point. If the point is inside the model, the push is inward, and if the point is outside, the push is outward (Figure 2.3).

This method is based on assumptions that the object boundary points and the local orientation (inside-outside) of the contour for each point can be determined. These assumptions actually can be easily fulfilled in the case of medical images, where an iso-contour generally suffices to define an object boundary and where the gradient defines the normal to that contour. In this case, the scene object contour is sampled into a given number of points, with the associated orientation, as shown in Figure 2.4.

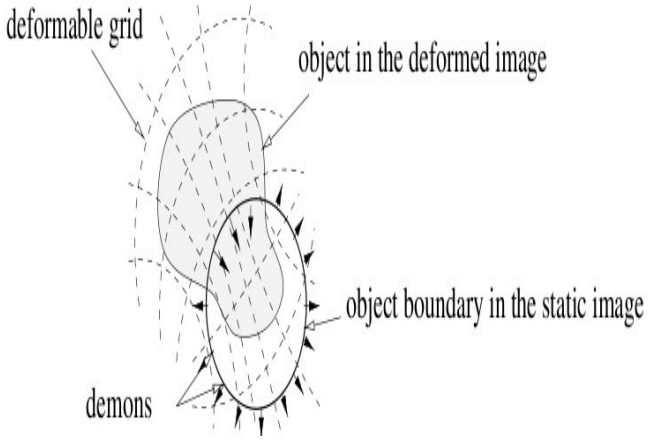

Figure 2.3. Diffusing models: a deformed image, considered as a deformable grid, is diffusing through the contours of the objects in the static image, by the action of effectors, called demons, situated in these interfaces (figure from [21]).

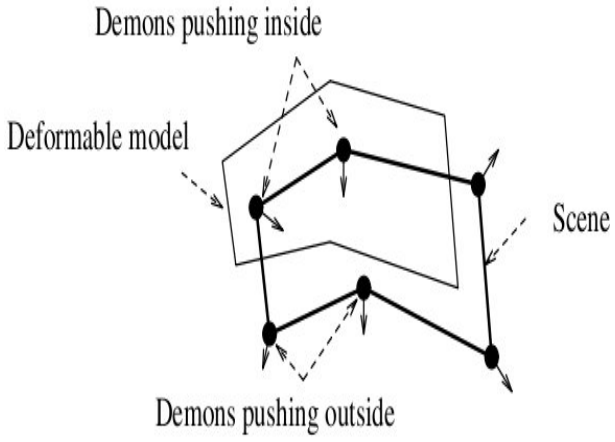

Figure 2.4. Deformable model with attractors (figure from [22]).

Intuitively, this tends to push the content of the model inside the object shape, while rejecting the background of the model image outside the shape. That is to say, this tends to sort inside and outside points of the model, with respect to the scene object interface, in the same way that Maxwell's demons sort two types of molecules of a mixed gas with respect to a semi-permeable membrane.

In Figure 2.5 upper two rows present three iterations of a standard attractor-based method (first line) and of the demon-based method (second line) applied to the rigid matching of two disks. In the case of attractor, forces originate from the boundary of the model (the moving disk), and are directed toward the closest point of the fix disk. In the case of demon, on the other hand, forces originate from the scene boundary (the static disk), and are directed outward or inward this disk, depending on whether the corresponding points are inside or outside the model disk. The force magnitudes decrease regularly in both cases. The force directions are different, meaning that the two methods are really different, and that this difference is not due to a change of the system of reference. Also, the attractor method necessitates the computation of closest points, which is not required by the demon method, and that the demon method necessitates the estimation of the inside and the outside, which is not required by the attractor method.

In Figure 2.5 lower two rows are other three iterations, and show that the behaviors of the two methods become similar (in that particular case) when coming close to the final solution.

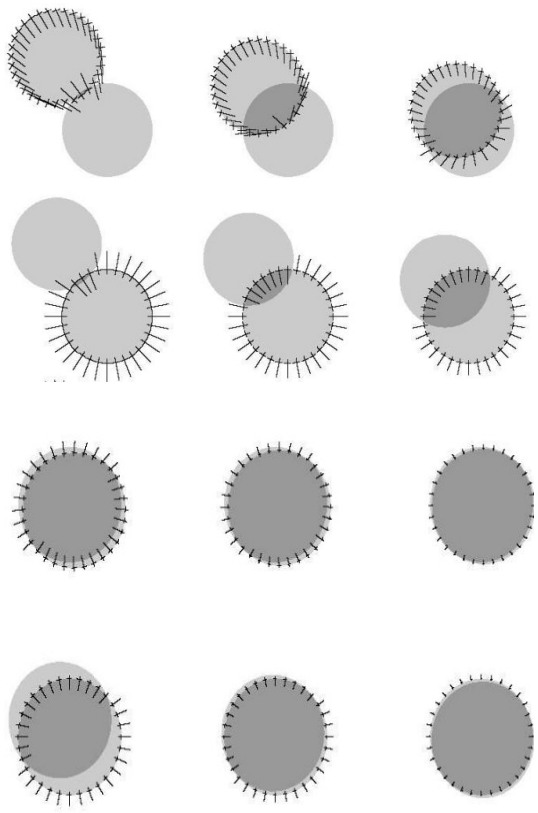

Figure 2.5. Next three iterations of the attractor-based method (upper row) and of the demon-based method (lower row) (figure from [21]).

3. METHODOLOGY

3.1. Overview of the Full Method

In this thesis, we used T1-weighted MR images of lower leg of human body in load and relaxation modes to serve as our test data. These 3D MR images of two different modes are the input fixed and moving images in our registration. There are two bone regions in human lower leg, tibia and fibula (Figure 3.1). In our proposed method, we performed the segmentation of these two bone regions, rigidly aligned and fixed the tibia, used the fibula to built an initial deformation field, which is used in performing our constrained elastic registration to obtain the final deformation field. We then used this final deformation field to perform strain analysis, by which we compare the performance of our newly proposed method with that of the existing fully elastic registration method. Figure 3.2 depicts the whole process of our constrained elastic registration method and Table 3.1 provides the notation used throughout the text. At

Figure 3.1. Illustration of tibia and fibula position in human body (courtesy Nucleus Communications, Inc.)

first, the tibia and fibula are segmented in both moving (I_M) and fixed (I_F) images to get the segmentation masks $\varphi_{t,M(X)}$, $\varphi_{t,F(X)}$, $\varphi_{f,M(X)}$ and $\varphi_{f,F(X)}$ for tibia and fibula respectively. Rigid registration parameters, θ_R, are found by registering $\varphi_{t,M(X)}$ and $\varphi_{t,F(X)}$ masks through rotation, shift and scaling. The whole moving image together

with $\varphi_{t,M(X)}$ and $\varphi_{f,M(X)}$ are rigidly transformed using θ_R to get $I_{M(X)'}$, $\varphi_{t,M(X)'}$ and $\varphi_{f,M(X)'}$. Then $\varphi_{f,M(X)'}$ is rigidly registered onto $\varphi_{f,F(X)}$ to get the initial registration parameter, $\theta_{R'}$, for the fibula region. The initial deformation field D_i, to be used by our constrained elastic registration, is built such that it is equal to the vector field given by $\theta_{R'}$ on fibula ($\varphi_{f,M(X)'}$) and zero elsewhere. Then the final registration is performed by applying the Demon's algorithm while keeping the tibia fixed (i.e. enforcing zero deformation vector field on tibia). The algorithm can be summarized as follows:

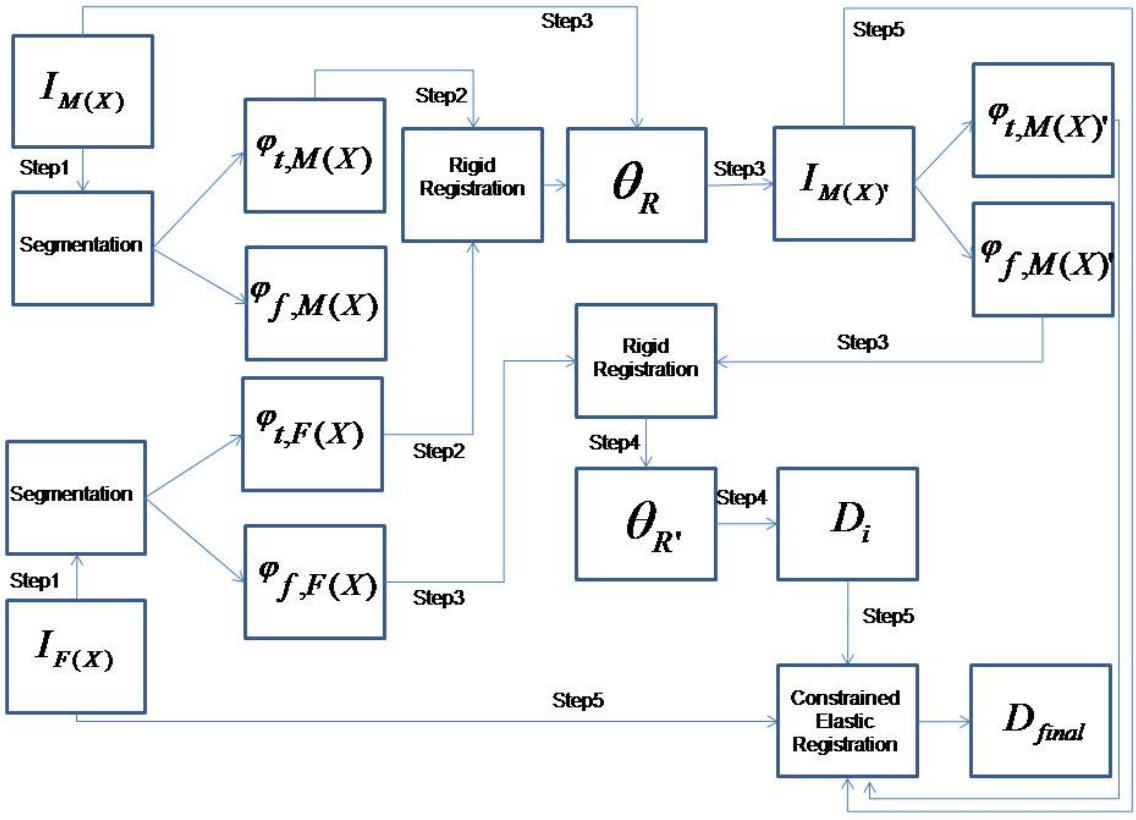

Figure 3.2. Flowchart of the full method

- Step1: Segment tibia & fibula in the moving and fixed images.
- Step2: Register the tibia rigidly.
- Step3: Determine the transformation parameters that rigidly registers fibula.
- Step4: Set the initial deformation vector field such that it is equal to the above determined rigid transformation on fibula and zero elsewhere.
- Step5: Perform elastic registration with the constraint that tibia is kept as fixed (the deformation field on tibia is forced to be zero).

Table 3.1. Meanings of Symbols used in the Flowchart of Full Method

Symbols	**Meaning**
$I_{M(X)}$	Moving original image
$I_{F(X)}$	Fixed original image
$\varphi_{t,M(X)}$	Segmented tibia mask of original moving image
$\varphi_{t,F(X)}$	Segmented tibia mask of original fixed image
$\varphi_{f,M(X)}$	Segmented fibula mask of original moving image
$\varphi_{f,F(X)}$	Segmented fibula mask of original fixed image
θ_R	Rigid registration parameters of $\varphi_{t,M(X)}$ and $\varphi_{t,F(X)}$
$I_{M(X)'}$	Transformed moving image by transforming $I_{M(X)}$ with P_R
$\varphi_{t,M(X)'}$	Segmented tibia mask of $I_{M(X)'}$
$\varphi_{f,M(X)'}$	Segmented fibula mask of $I_{M(X)'}$
$\theta_{R'}$	Rigid registration parameters of $\varphi_{f,M(X)'}$ and $\varphi_{f,M(X)}$
D_i	Initial vector space built by $\theta_{R'}$
D_{final}	Final deformation field obtained by our proposed method

3.2. Tibia and Fibula Segmentation

The tibia and fibula regions of test datasets are segmented with the *Isolated Connected Component* [23] method. The main reason for choosing Isolated Connected Component method for our segmentation is that the intensity difference between bone regions and its surrounding tissues in our test data sets is big, which is very suitable to be separated effectively by threshold.

In *Isolated Connected Component* method, the input values are the coordinates of two seed points, P_1 and P_2, together with one lower threshold value T_l. We choose one seed point P_1 in the bone region and the other seed point P_2 in its surrounding dark region (as shown in Figure 3.3). The algorithm then starts to evolve from these two given points, and obtains two different regions, R_1 and R_2 that are having intensities higher than T_l:

$$R_1 > T_l, R_2 > T_l, R_1 \cap R_2 = \emptyset \tag{3.1}$$

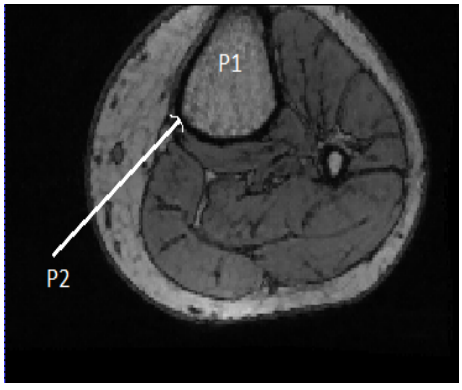

Figure 3.3. Positions of two provided segmentation seeds, P_1 and P_2.

The upper threshold is determined automatically using binary search such that the final resulted region is connected to first seed, and not to second seed. The final

segmentation mask is our R_1 here.

Figure 3.4 shows one slice of our test dataset and its obtained tibia segmentation mask shown as an example:

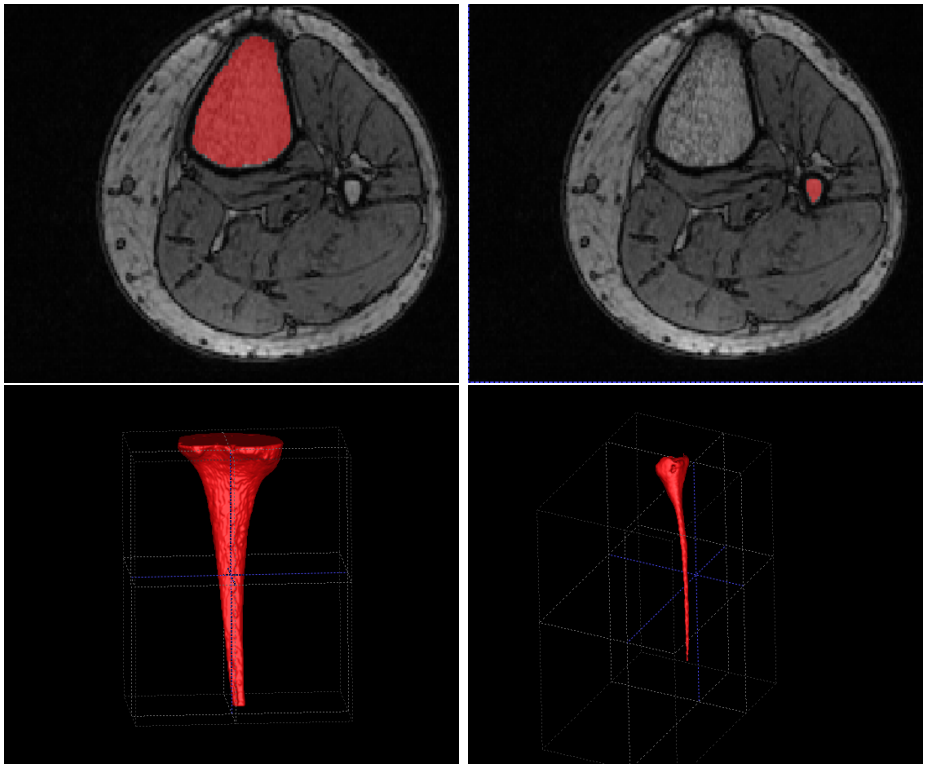

Figure 3.4. Segmentation of tibia and fibula on T1 weighted MRI are shown (in red) in 2D axial slices and 3D volume. Left column shows tibia, right column shows fibula.

3.3. Registration

3.3.1. Rigid Registration

The basic inputs of the registration process are two images: one is defined as the *fixed image* $I_{F(X)}$, and the other as the *moving image* $I_{M(X)}$, in which X represents a position in N-dimensional space. The static image is acquired under relaxation mode, and moving image is acquired when the hip and knee joints were brought in flexion by repositioning the upper body by a chest support. The detailed information for acquiring these datasets are given in Chapter 4.

Registration is regarded as an optimization problem with the goal of finding the spatial mapping that will bring the moving image into alignment with the fixed image [24]. The transformation:

$$\underline{T}(X;\theta) : \Re^3 \rightarrow \Re^3 \tag{3.2}$$

represents the spatial mapping of points from the moving image space to points in the fixed image space, in which, θ represents transformation parameters, and X is a 3D point. The L1-norm based cost function in terms of intensity differences is:

$$F(I_{M(X)}, I_{F(X)}; \underline{T}(X;\theta)) = \sum_{X \in \Omega} |I_{M(\underline{T}(X;\theta))} - I_{F(X)}| \tag{3.3}$$

where Ω is the image space. The registration is to find an optimal θ such that

$$\theta^* = \arg\min_{\theta} F \tag{3.4}$$

$$\underline{T}^* = \underline{T}(X;\theta^*) \tag{3.5}$$

Our rigid registration process is based on the 3D versor transformation, in which the moving image is transformed according to:

$$I_{M(X')} = V \cdot |I_{M(X)} - I_{F(X)}| + I_{F(X)} \tag{3.6}$$

where $I_{M(X)}$ and $I_{M(X')}$ are the moving image intensity before and after transformation respectively, $I_{F(X)}$ is the fixed image, and V is the versor between moving and fixed images before transformation. This could further become as:

$$I_{M(X')} = V \cdot I_{M(X)} + \underline{T}(X;\theta) \tag{3.7}$$

$$\underline{T}(X;\theta) = I_{F(X)} - V \cdot I_{F(X)} \tag{3.8}$$

where θ of the transformation $\underline{T}(X;\theta)$ include the rotation and translation parameters. This registration is optimized by using gradient optimizer and the parameters are updated as follows:

$$\theta^{'} = \theta + \frac{\partial F}{\partial \theta}\lambda \tag{3.9}$$

$$V' = V \exp(G)^{\lambda} \tag{3.10}$$

where $\theta^{'}$ and V' are the updated transformation parameters and versor respectively, F is the cost function, G is the variation from the gradient of the cost function, and λ is the step length of the algorithm. The step length λ can be any value between $0 < \lambda < 1$ but most cases it is taken between 0.01 to 0.001. The implementation of our rigid registration is based on *The Insight Toolkit* (ITK) [25], and its built-in gradient optimizer gives us 0.01 for λ here.

We used the parameter θ of this rigid registration, which includes translation and rotation parameters, to build the initial deformation vector field for our proposed constrained elastic registration.

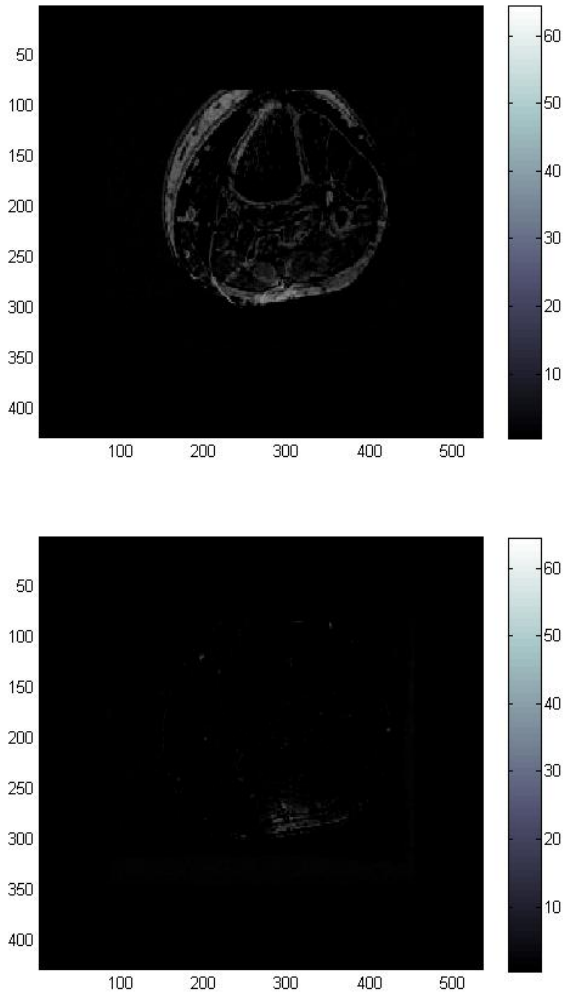

Figure 3.5. Difference between original moving and fixed image before (upper) and after (lower) rigid registration.

3.3.2. Constrained Elastic Registration

In this step, we perform Demons based constrained elastic registration in which we keep the tibia region as rigid, and then elastically register the remaining part for our test data. Here in our work, lower leg is the target region.

The orientation and magnitude of the displacement is derived from the instantaneous optical flow equation [25]:

$$D(X) \cdot \nabla I_{F(X)} = -(I_{M(X)} - I_{F(X)}) \tag{3.11}$$

where $I_{F(X)}$ is the fixed image, $I_{M(X)}$ is the moving image to be registered, ∇ denotes gradient and $D(X)$ is the displacement or optical flow between the images. It is well-known that Equation 3.11 is insufficient to specify $D(X)$ locally and is usually determined using some form of regularization. The projection of the vector on the direction of the intensity gradient is used in the registration process

$$D(X) = \frac{-(I_{M(X)} - I_{F(X)})\nabla I_{F(X)}}{||\nabla I_{F(X)}||^2} \tag{3.12}$$

However, when the image gradient is small, this equation becomes unstable and result in large displacement values. To solve this problem, Thirion [21, 22] re-normalizes the equation such that:

$$D(X) = \frac{-(I_{M(X)} - I_{F(X)})\nabla I_{F(X)}}{\|\nabla I_{F(X)}\|^2 + (I_{M(X)} - I_{F(X)})^2/K} \tag{3.13}$$

where K is a normalization factor that accounts for the units imbalance between intensities and gradients, and is computed as the mean squared value of the pixel spacing. The inclusion of K makes the force computation to be invariant to the pixel scaling of the images.

The initial deformation vector field D_i serves as the initial deformation field $D^0(X)$ in our constrained elastic registration alogrithm. The segmentation mask of

the tibia for the moving image serves as the rigid region mask. The demons algorithm iteratively updates the initial deformation vector field using Equation 3.13, unless it is in the tibia mask, as follows:

$$D^N(X) = D^{N-1}(X) - \frac{(I_{M(X+D^{N-1}(X))} - I_{F(X)})\nabla I_{F(X)}}{\|\nabla I_{F(X)}\|^2 + (I_{M(X+D^{N-1}(X))} - I_{F(X)})^2} \tag{3.14}$$

where N is the nth iteration. In each iteration, the moving image pixel gets deformation from previous iteration, and its position becomes $X + D^{N-1}(X)$, and with this new position, the difference between moving and fixed images further becomes as $I_{M(X+D^{N-1}(X))} - I_{F(X)}$. Thus, after each iteration, moving image is constructed again according to the displacement values and then new D is calculated accordingly, and the algorithm tries to decrease the dissimilarity by subtraction with previous deformation by which total displacement of each pixel is updated. After the iteration number N reaches a provided value, or the total difference between images becomes smaller than a threshold value prescribed, the algorithm stops, and the last updated value of the total displacement gives us the displacement value of each pixel. Thus the Demons algorithm gives the alignment information of fixed and moving images by means of gradients and difference between fixed and moving images.

The implementations of the segmentation and registration methods we used are done with the help of freely available open source library *The InsightToolKit* [26].

3.4. Experiments

3.4.1. Test Subjects

Experimental procedures were in strict agreement with guidelines and regulations concerning human welfare and experimentation set forth by Turkish law, and approved by the Committee on Ethics of Human Experimentation at Istanbul University, Istanbul School of Medicine, Istanbul. Five healthy subjects ((mean±SD): age = 27±3 years, height = 175±7cm and body mass = 73±8 kg) volunteered for this study. Only

males were recruited so that anthropometric differences between subjects are minimized. After a full explanation of the purpose and methodology of the experiments, these subjects provided an informed consent.

3.4.2. Experimental Protocol

During the experiment, each subject was positioned prone within the MRI scanner. The target (left) leg of the subject was brought to a reference position before the patient table (a motorized and computer-controlled slide carrying the patient) was moved into the MRI bore: (i) the ankle angle was fixed at 90° by using an MRI compatible ankle-foot orthosis (brace on the lower leg and the foot allowing fixation of the ankle angle). (ii) In order to keep orientation of the lower leg within the MRI scanner constant, the position of the knee cap and the tip of the ankle-foot orthosis were marked on the MRI patient table. (iii) The knee angle in this prone position with fixed ankle angle (referred to as the *undeformed state*) was (mean ± SD) 173° ± 3°. After moving the patient table into the bore, sets of 3D high resolution MR images were acquired in the undeformed state. Subsequently, the patient table was moved out of the bore. The hip and knee joints were brought in flexion by repositioning the upper body by a chest support using MRI compatible positioning aids, the trunk was elevated until reaching the spatial limits of the MRI bore (diameter = 60 cm). In this *deformed state*, the knee angle equaled 150° ± 6°. Care was taken to maintain the positions of the knee cap and the tip of the ankle-foot orthosis using the markers drawn previously on the patient table. Subsequently, the patient table was moved back into the bore automatically ensuring that it attains the identical position it attained during acquisition of the image set in the *undeformed state* and a second MR image set was collected.

We used a localizer (i.e. just before acquisition of main images low resolution pilot image acquired fast to select the volume to be imaged) to first select the region between the most proximal part of the fibula and the most proximal location of the transverse crural ligament to be imaged and also to align manually the central axis of the tibia with the longitudinal direction. Then, using a 3T Siemens Trio scanner

with 6-channel surface cardiac array coil (matrix size = 250x220x144, voxel size = 0.75x0.75x0.8 mm, TR = 2000 ms, TE = 3.94 ms, no fat suppression, flip angle = 12°, bandwidth = 130 Hz per pixel), we collected 3D Turbo Flash based coronal MR image sets for each test subject. These data sets are used as input data sets for our calculation of tissue strain analysis.

A "synthetic rigid body motion" was imposed on the data for each subject of image sets of the undeformed state so as to transform it: (i) a 10^0 rotation within the cross-sectional plane (corresponding to an endorotation of knee as the knee flexed), (ii) a 3° rotation in the coronal plane, (iii) a 3° rotation in the sagittal plane and (iv) a 4mm translation in the axial direction. By doing this, we obtained a new data set that is similar to the deformed state obtained by our scanner, the difference is, here after synthetic rigid body motion, we manually get a new deformed state. This manually obtained deformed state and the original deformed state obtained by our scanner are used as the input datasets for our registration framework to calculate baseline strain values.

Thus, we have five different test data sets including undeformed and deformed data sets for each of them. After imposing synthetic rigid body motion to the undeformed data sets, and manually obtaining new five deformed data sets, we perform our registration between the original deformed data set and the manually deformed data set, then calculate their strains, which is regarded as *baseline strains*. The baseline strain value reveals the limit and calculation error percentage of our algorithm.

We also use the original *undeformed* and *deformed* data sets to perform our registration again and from the obtained deformation field, we calculate corresponding *tissue strains* for these original five different groups. That is to say, the baseline strain is calculated from the *deformed* data sets manually obtained by using computer and the original *deformed* data set while the tissue strain is calculated from the original *undeformed* and *deformed* data sets.

4. RESULTS

4.1. Qualitative Assessment of Segmentation

We used *Isolated Connected Component* method, which is described in Chapter 3, to perform segmentation on tibia and fibula of our test data. The lower threshold values range from 80 to 160 and is selected empirically by subjective and visual evaluation of resultant segmentation masks. The processing time is varying between half to one minute for tibia, and 15 to 40 seconds for fibula on a workstation with 4x2.66GHz CPU, and 8Gb memory under Ubuntu operating system. The obtained segmentation results are illustrated in the Figures 4.1 and 4.2, together with manually segmented results for comparison. The manually segmented masks are obtained after consulting with one professional doctor from Yeditepe University hospital in Istanbul, Turkey. By visual inspection, we can see that our segmentation algorithm gives similar results to those manually obtained segmentation masks. The Figure 4.3 shows the 3D visualization of our segmented tibia and fibula masks together from one of our test datasets.

4.2. Quantitative Analysis of Deformation Field

The focus of our work is to carry out muscle strain analysis from registration of MR images of lower leg of human body, in which we compare strain measurements obtained by the proposed constrained elastic registration with that of the fully elastic registration. Before getting into the strain analysis results, it is worth mentioning the definition of strain in deformation.

4.2.1. Strain in Deformation

Strain is defined as the deformation per unit length. For instance, if we have a rod of length L, and used a force to cause a deformation of δ in that rod, the strain ϵ

Figure 4.1. Segmentation of tibia (shown in red) on T1 weighted MRI are shown in 2D sagittal slices and 3D volume. Left column shows the result of our employed segmentation method, right column shows the result of manual segmentation for comparison. We can see that our segmentation method gives similar result to that of manual segmentation.

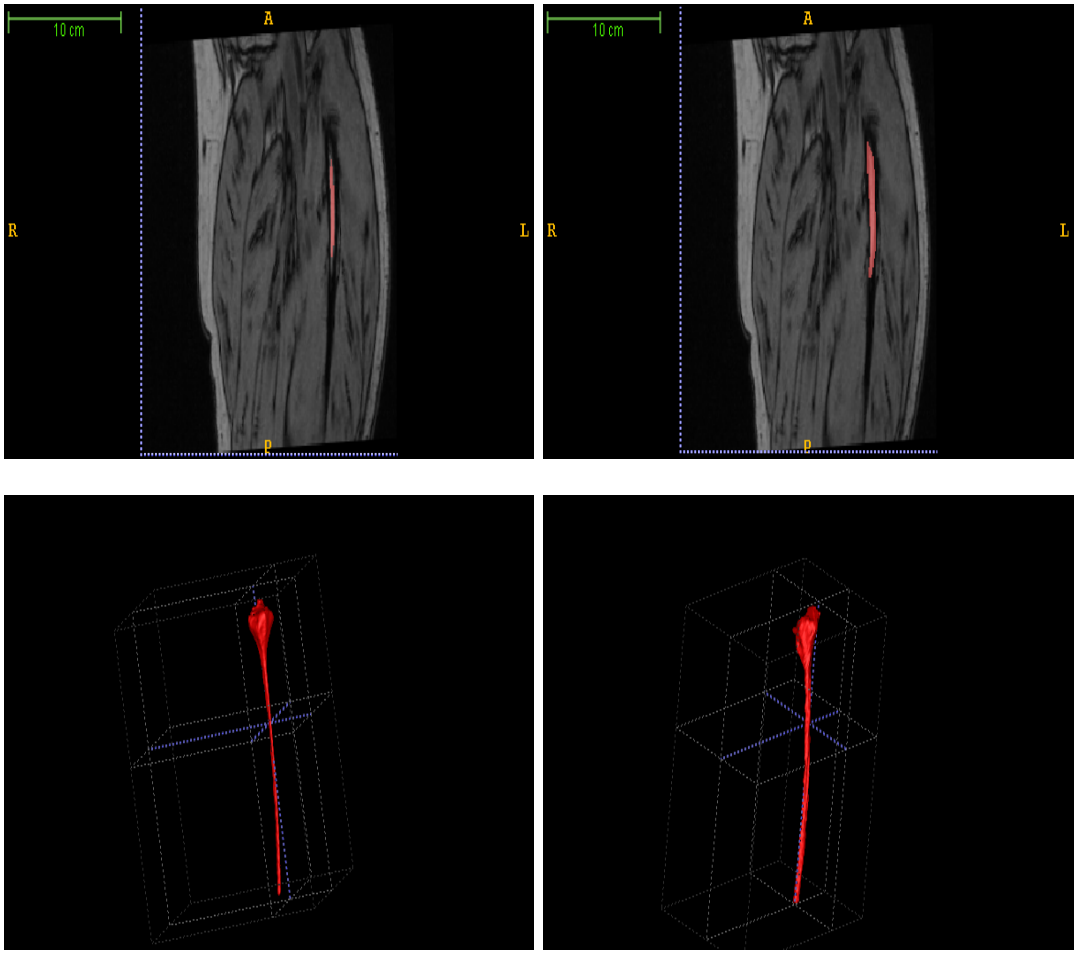

Figure 4.2. Segmentation of fibula (shown in red) on T1 weighted MRI are shown in 2D sagittal slices and 3D volume. Left column shows the result of our employed segmentation method, right column shows the result of manual segmentation for comparison. We can see that our segmentation method gives similar result to that of manual segmentation.

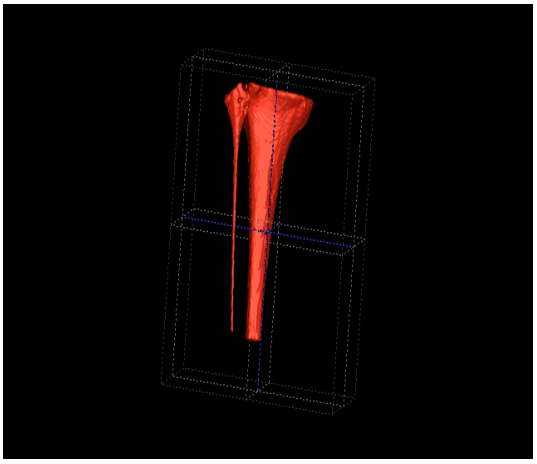

Figure 4.3. 3D visualization of both segmented bones.

could be written as:

$$\epsilon = \delta / L \tag{4.1}$$

Thus, strain has no unit.

Using displacement fields obtained by our constrained elastic registration, a Green-Lagrange strain tensor is computed for each voxel in order to assess deformations within the lower leg muscles present after changing the knee and hip angles.

To calculate the strain tensor, the deformation gradient matrix F, characterizing the voxel deformation, was calculated first by using the displacement gradient(∇u) [27],

$$F = \nabla u + I \tag{4.2}$$

in which, I is identity matrix such that:

$$I = \begin{bmatrix} 1 & 0 & 0 \\ 0 & 1 & 0 \\ 0 & 0 & 1 \end{bmatrix} \tag{4.3}$$

Then, the Green-Lagrange strain tensor, E, is given as:

$$E = \frac{1}{2}[F^T F - I] \tag{4.4}$$

Example of the calculation of one strain value between neighboring pixels is given as follows: consider we have a deformed square consisting of four points as shown in Figure 4.4. The displacement values of these four points are those calculated by Demons algorithm.

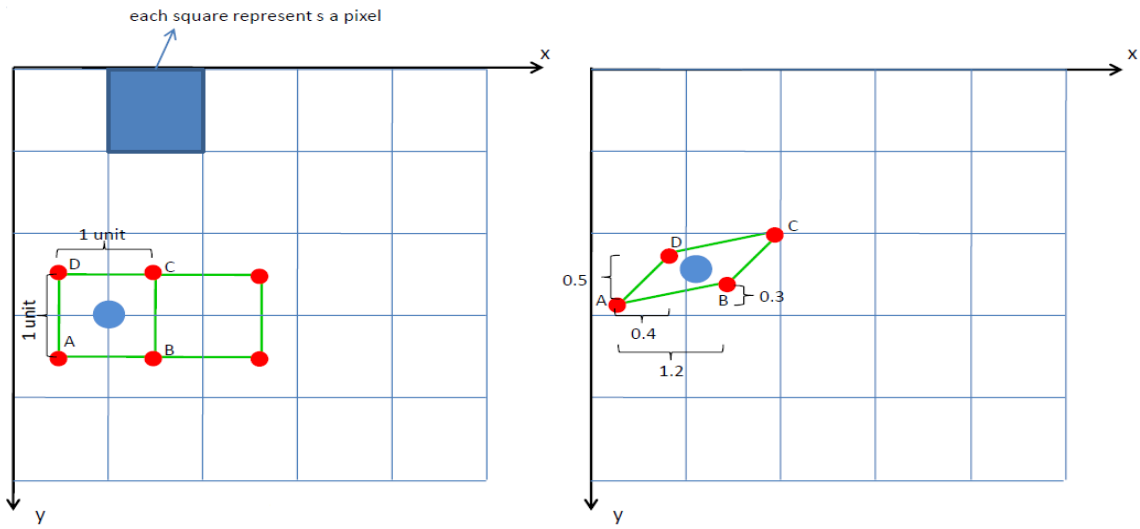

Figure 4.4. The red circles (A,B,C,D) are centers of the four neighboring pixels and the big blue circle is the center of the square (ABCD) on the left. On the right the square (ABCD) is deformed according to the displacements of the four points (i.e. A,B,C,D)

1.2 and 0.5 are the new lengths in x and y axes, respectively. 0.3 and 0.4 are the shear values. Using these four values we can set "deformation gradient matrix" as:

$$F = \begin{bmatrix} 1.2 & 0.4 \\ 0.3 & 0.5 \end{bmatrix} \tag{4.5}$$

From Equation 4.4, strain matrix is calculated as:

$$E = \begin{bmatrix} 0.27 & 0.32 \\ 0.32 & -0.30 \end{bmatrix} \tag{4.6}$$

The diagonal elements (i.e. 0.27 and -0.30) are normal strains and 0.32 is the shear strain. In our case, we only focus on normal strains since it gives us the maximum lengthening.

4.2.2. Strain Analysis Results

A slice group consisting of 30 consecutive cross-sectional slices was selected manually for each subject (left of Figure 4.4). The most proximal slice location was at the proximal third of the length of imaged portion of the lower leg. For each slice analyzed, we divided the lower leg muscles into five groups according to the physiological characters (right of Figure 4.4): Gastrocnemius (GM) , Soleus (SOL), Deep Flexors (DF), Peronei (PER), and Anterior Crural (AC) muscle group. The main reason for us to use these five muscle groups is that according to the common view, after knee angle changes, as in our case, there should only be deformation in GM muscle region. But recent studies have shown that in fact deformation can be observed not only in GM, but also in SOL, DF, AC and PER muscle regions as well [4,27]. That means the myofascial force that is generated under lower leg is transferred throughout the muscle region and caused deformation. Thus, in order to carry out further analysis of force transmission more accurately among muscle, these five groups are chosen.

We calculated the baseline and tissue strains for these five different muscle groups. We also calculated the baseline and tissue strains for border regions of these groups and regions away from the borders, so as to avoid the effects caused by the borders. It was shown out that the deformed tissue continues its deformation within three voxel distance from it [27], by using the datasets that have same voxel sizes with our datasets. Thus, we chose the muscle groups' border width as three pixel for each slice. The borders are obtained by moving a 3x3 window along the border lines of these

manually selected five muscle groups.

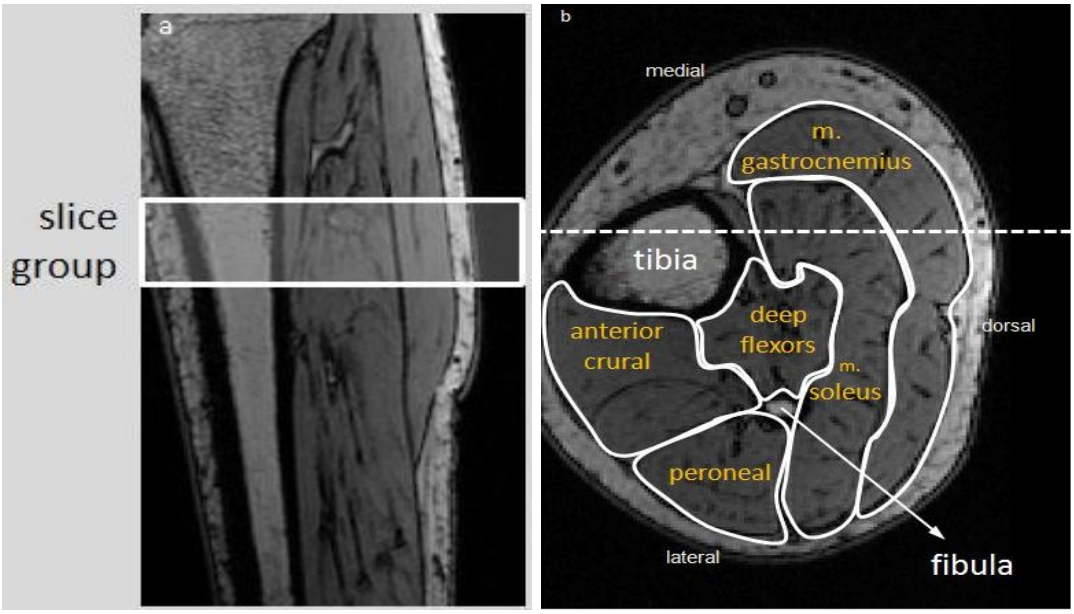

Figure 4.5. Left: illustration of the locations of the group of cross-sectional slices (white solid rectangle) to be analyzed for strains [27]. Right: five anatomical regions of interest were distinguished: m.gastrocnemius, m.soleus, deep flexor muscles, peroneal muscles and anterior crural muscles. The dashed horizontal line indicates the location of sagittal image shown in left

The calculated baseline strain values using deformation field that come from registering manually obtained *deformed* state data sets with original *deformed* state data sets are given in the Table 4.1. The table report the baseline strain values' mean and standard deviation within the corresponding manually masked muscle volumes for each one of five subjects.

Explanation of the contents of Table 4.1: the 'Subjects' column indicates the five different test data sets we used in our work, labeled as A, B, C, D and E. The GM, SOL, DF, PER and AC refer to the muscle group regions that are obtained after our manually division of the lower leg muscles of our test data sets. The inside values in the table are mean values of the calculated baseline strain values and their standard deviations for complete muscle, muscle boundaries and muscle interior. The main

reason for calculating strain values for muscle boundaries and interiors is to avoid the boundary effect. The 'mean value' means we calculate baseline strains for the five muscle groups separately for 30 slices and take average of them. The approximate size of these five muscle group regions for 30 slices are as follows: for 'GM' region there is around '84730' pixels, for 'SOL' region there is around '74560' pixels, for 'DF' region there is around '37725' pixels, for 'PER' region there is around '33690' pixels, and for 'AC' region there is around '53780' pixels for 30 slices that we choose to calculate strain values. For instance, the mean value of calculated baseline strain value for test data set A for 'GM' muscle group region in complete muscle is '0.0149', this means the baseline strain values for around '84730' pixels for totally 30 slices have a mean value of '0.0149', and standard deviation of '0.0201'. The population mean, *Mean*, means the mean values of each column. For instance, for 'GM' region for complete muscle, the mean of '0.0212', '0.0183', '0.0234', '0.0210', and '0.0261' gives '0.0220', and the mean of those standard deviations, namely '0.0149', '0.0135', '0.0193', '0.0140', and '0.0242' gives '0.0029'. The remaining parts of the table are in the same manner, as well as the remaining tables' contents.

By subtracting the baseline strain values of muscle boundaries with values of muscle interiors, we get the Table 4.2. The difference values will be used for our discussion of the relationship between regions away from borders and border regions later in our 'Discussion' part in Chapter 5. The difference values shown in Table 4.4 are also obtained in the same manner.

Table 4.1. Mean ± Standard Deviation Values of Baseline Strains for Unconstrained Elastic Registration Method (R1: complete muscle, R2: muscle boundaries, R3: muscle interior)

Subjects		GM	SOL	DF	PER	AC
A	R1	0.0212±0.0149	0.0201±0.0128	0.0154±0.0084	0.0179±0.0116	0.0231±0.0180
	R2	0.0361±0.0170	0.0223±0.0129	0.0147±0.0084	0.0247±0.0128	0.0249±0.0224
	R3	0.0201±0.0143	0.0199±0.0128	0.0155±0.0084	0.0172±0.0113	0.0230±0.0176
B	R1	0.0183±0.0135	0.0157±0.0101	0.0138±0.0081	0.0133±0.0078	0.0129±0.0094
	R2	0.0313±0.0174	0.0186±0.0101	0.0156±0.0071	0.0182±0.0090	1.1017±4.5299
	R3	0.0174±0.0128	0.0155±0.0100	0.0137±0.0082	0.0129±0.0076	0.0121±0.0082
C	R1	0.0234±0.0193	0.0157±0.0101	0.0138±0.0073	0.0146±0.0088	0.0175±0.8891
	R2	0.0778±0.0637	0.0217±0.0110	0.0139±0.0072	0.0209±0.0126	1.6116 ± 6.9853
	R3	0.0224±0.0182	0.0153±0.0099	0.0138±0.0073	0.0141±0.0084	0.0161±0.0118
D	R1	0.0210±0.0140	0.0177±0.0107	0.0162±0.0084	0.0147±0.0088	0.0169±0.0104
	R2	0.0344±0.0158	0.0215±0.0104	0.0162±0.0086	0.0218±0.0114	0.0236±0.0154
	R3	0.0203±0.0136	0.0175±0.0107	0.0162±0.0084	0.0142±0.0084	0.0164±0.0118
E	R1	0.0261±0.0242	0.0144±0.0088	0.0150±0.0084	0.0140±0.0087	0.0225±0.0156
	R2	0.0437±0.0393	0.0188±0.0092	0.0157±0.0080	0.0216±0.0135	0.0271±0.0192
	R3	0.0250±0.0230	0.0141±0.0087	0.0150±0.0085	0.0133±0.0081	0.0223±0.0153
Mean±STD	R1	0.0220±0.0029	0.0167±0.0022	0.0148±0.0010	0.0149±0.0018	0.0186±0.0042
	R2	0.0447±0.1566	0.0206±0.0107	0.0152±0.0079	0.0214±0.0118	0.5578±2.3144
	R3	0.0210±0.0164	0.0165±0.0104	0.0148±0.0082	0.0143±0.0088	0.0180±0.0126

Table 4.2. Difference in Mean Values of Baseline Strains Between Regions Away From Borders and Border Regions for Unconstrained Elastic Registration Method

Subjects	**GM**	**SOL**	**DF**	**PER**	**AC**
A	-0.0160	-0.0024	0.0008	-0.0075	-0.0019
B	-0.0139	-0.0031	-0.0019	-0.0053	-1.0896
C	-0.0554	-0.0064	-0.0001	-0.0068	-1.5955
D	-0.0141	-0.0040	0	-0.0076	-0.0072
E	-0.0187	-0.0047	-0.0007	-0.0083	-0.0048
$\overline{Mean}$	-0.0236	-0.0041	-0.0004	-0.0071	-0.5398

Table 4.3. Mean ± Standard Deviation Values of Baseline Strains for Constrained Elastic Registration Method (R1: complete muscle, R2: muscle boundaries, R3: muscle interior)

Subjects		GM	SOL	DF	PER	AC
A	R1	0.0271±0.0202	0.0245±0.0164	0.0167±0.0101	0.0205±0.0140	0.028±0.0202
	R2	0.0446±0.0231	0.0261±0.0157	0.0160±0.0096	0.0282±0.0158	0.0293±0.0271
	R3	0.0257±0.0195	0.0244±0.0165	0.0168±0.0101	0.0197±0.0136	0.0279±0.0197
B	R1	0.0254±0.0198	0.0214±0.0144	0.0173±0.0109	0.0166±0.0104	0.0158±0.0123
	R2	0.0410±0.0226	0.0258±0.0143	0.0210±0.0098	0.0257±0.0133	0.0399±0.0370
	R3	0.0243±0.0192	0.0210±0.0143	0.0171±0.0109	0.0159±0.0099	0.0146±0.0108
C	R1	0.0275±0.0217	0.0218±0.0149	0.0154±0.0086	0.0155±0.0096	0.0206±0.0158
	R2	0.0441±0.0358	0.0264±0.0139	0.0150±0.0081	0.0231±0.0147	0.0343±0.0343
	R3	0.0264±0.0208	0.0215±0.0149	0.0154±0.0087	0.0149±0.0091	0.0197±0.0147
D	R1	0.0285±0.0196	0.0248±0.0158	0.0184±0.0100	0.0171±0.0111	0.0214±0.0143
	R2	0.0446±0.0213	0.0261±0.0137	0.0175±0.0100	0.0244±0.0133	0.0280±0.0199
	R3	0.0203±0.0136	0.0175±0.0107	0.0162±0.0084	0.0142±0.0084	0.0164±0.0118
E	R1	0.0276±0.0192	0.0247±0.0159	0.0184±0.0100	0.0165±0.0107	0.0209±0.0139
	R2	0.0352±0.0208	0.0229±0.0114	0.0191±0.0098	0.0271±0.0173	0.0360±0.0242
	R3	0.0235±0.0161	0.0189±0.0125	0.0184±0.0116	0.0166±0.0107	0.0335±0.0232
Mean±STD	R1	0.0265±0.0017	0.0223±0.0023	0.0173±0.0013	0.0174±0.0019	0.0239±0.0069
	R2	0.0419±0.0247	0.0255±0.0138	0.0177±0.0095	0.0257±0.0149	0.0335±0.0285
	R3	0.0255±0.0190	0.0221±0.0148	0.0172±0.0103	0.0167±0.0108	0.0233±0.0164

Table 4.4. Difference in Mean Values of Baseline Strains Between Regions Away From Borders and Border Regions for Constrained Elastic Registration Method

Subjects	**GM**	**SOL**	**DF**	**PER**	**AC**
A	-0.0189	-0.0017	0.0008	-0.0085	-0.0014
B	-0.0167	-0.0048	-0.0039	-0.0098	-0.0253
C	-0.0177	-0.0049	0.0004	-0.0082	-0.0146
D	-0.0170	-0.0014	0.0009	-0.0079	-0.0071
E	-0.0017	-0.0040	-0.0007	-0.0105	-0.0025
$\overline{Mean}$	-0.0164	-0.0034	-0.0005	-0.0090	-0.0102

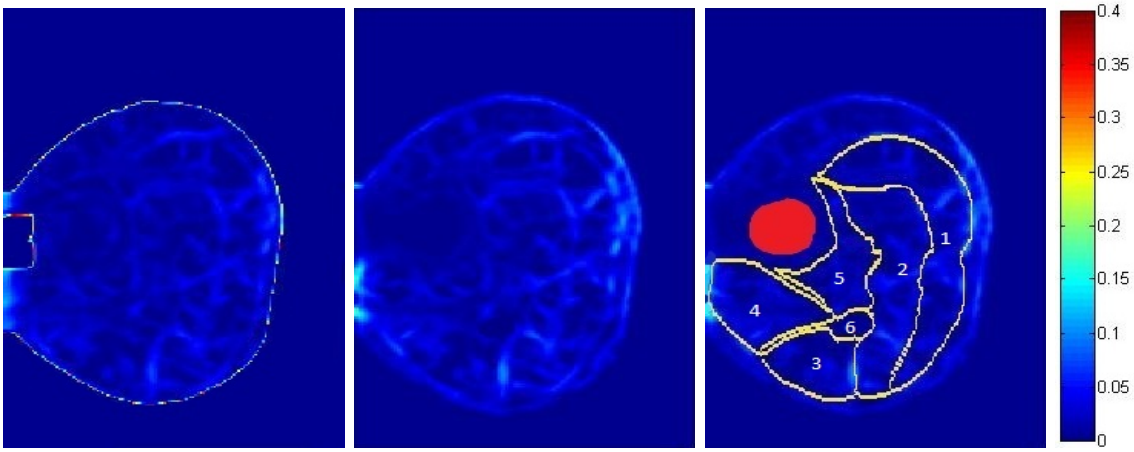

Figure 4.6. 1st slice of Baseline strain maps of Test Subject "A" Left: result from fully elastic registration method Middle: result from our proposed constrained elastic registration method Right: result from our proposed constrained elastic registration with muscle group borders (1:GM,2:SOL,3:PER,4:AC,5:DF,6:fibula) and tibia segmentation mask in red color shown on it.

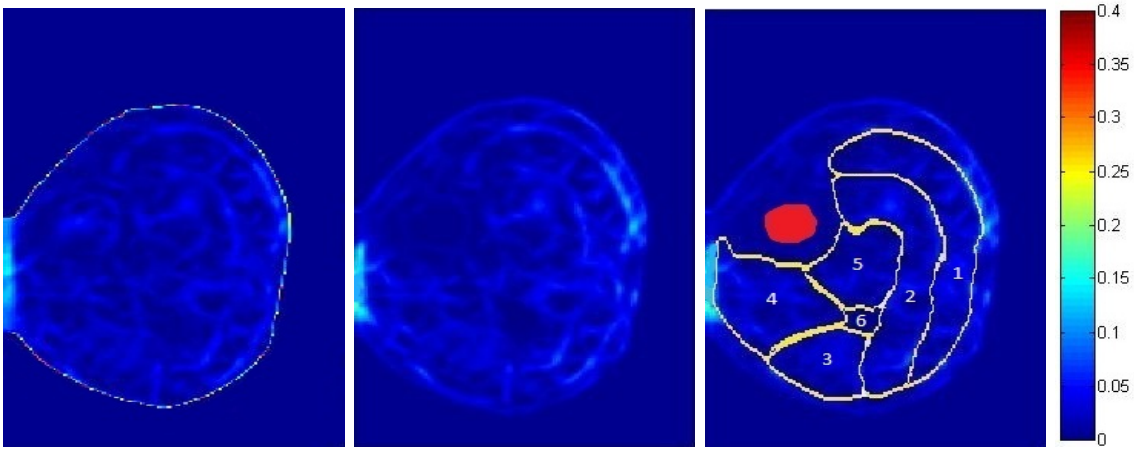

Figure 4.7. 30th slice of Baseline strain maps of Test Subject "A" Left: result from fully elastic registration method Middle: result from our proposed constrained elastic registration method Right: result from our proposed constrained elastic registration with muscle group borders (1:GM,2:SOL,3:PER,4:AC,5:DF,6:fibula) and tibia segmentation mask in red color shown on it.

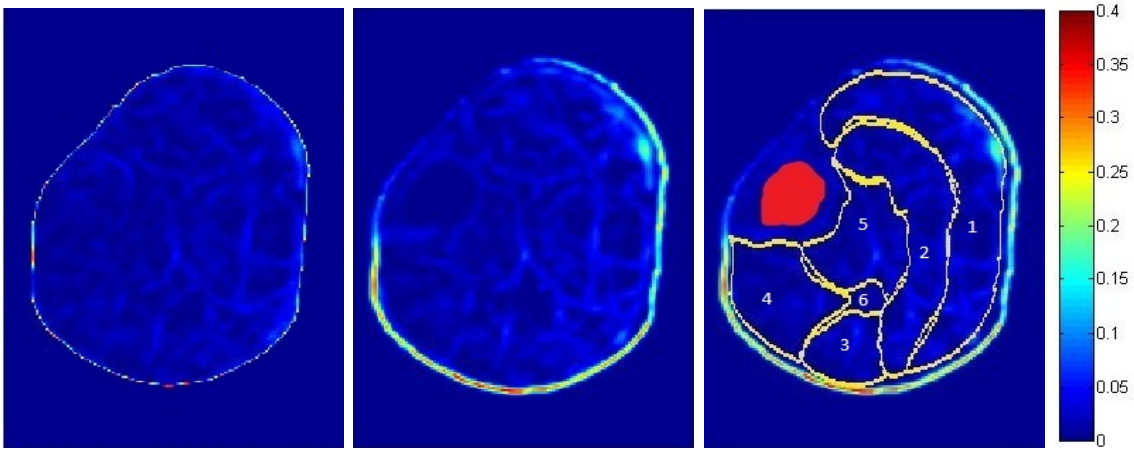

Figure 4.8. 1st slice of Baseline strain maps of Test Subject "B" Left: result from fully elastic registration method Middle: result from our proposed constrained elastic registration method Right: result from our proposed constrained elastic registration with muscle group borders (1:GM,2:SOL,3:PER,4:AC,5:DF,6:fibula) and tibia segmentation mask in red color shown on it.

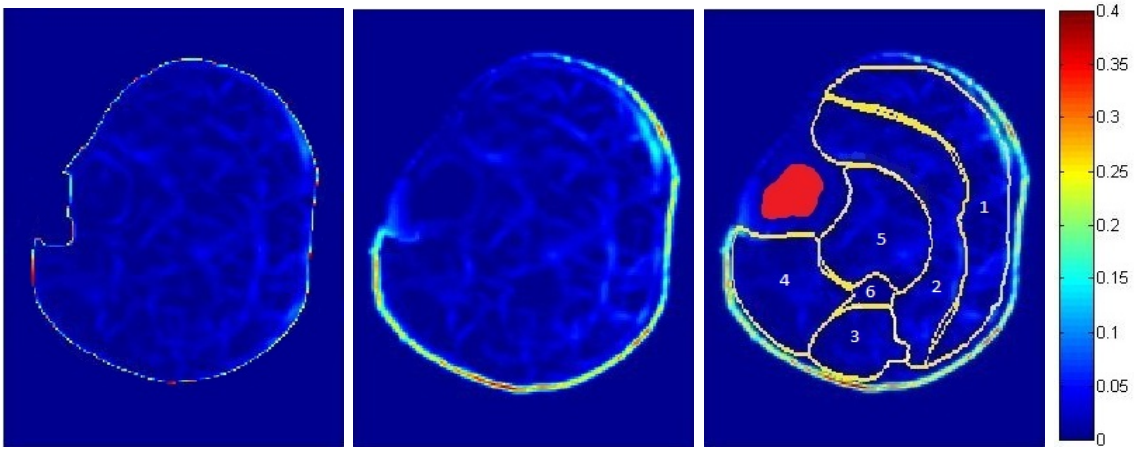

Figure 4.9. 30th slice of Baseline strain maps of Test Subject "B" Left: result from fully elastic registration method Middle: result from our proposed constrained elastic registration method Right: result from our proposed constrained elastic registration with muscle group borders (1:GM,2:SOL,3:PER,4:AC,5:DF,6:fibula) and tibia segmentation mask in red color shown on it.

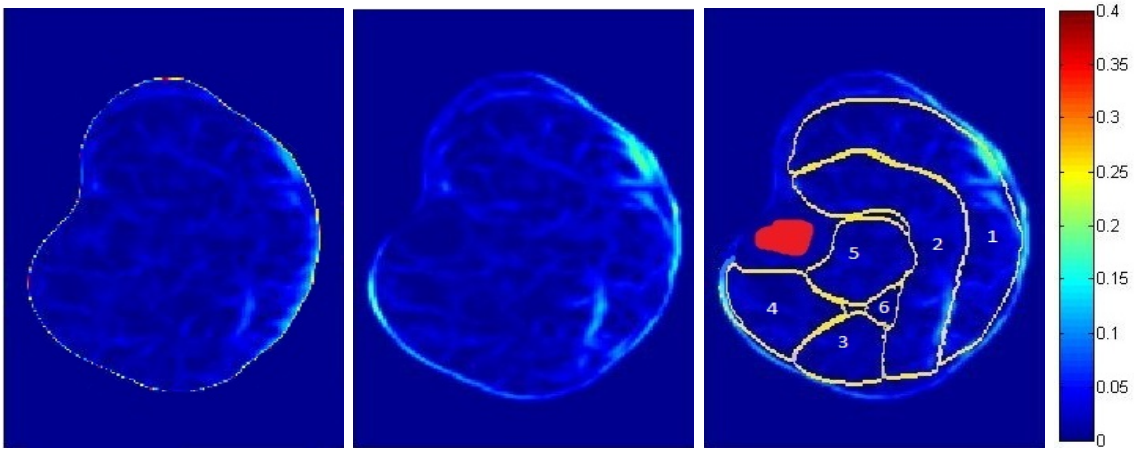

Figure 4.10. 1st slice of Baseline strain maps of Test Subject "C" Left: result from fully elastic registration method Middle: result from our proposed constrained elastic registration method Right: result from our proposed constrained elastic registration with muscle group borders (1:GM,2:SOL,3:PER,4:AC,5:DF,6:fibula) and tibia segmentation mask in red color shown on it.

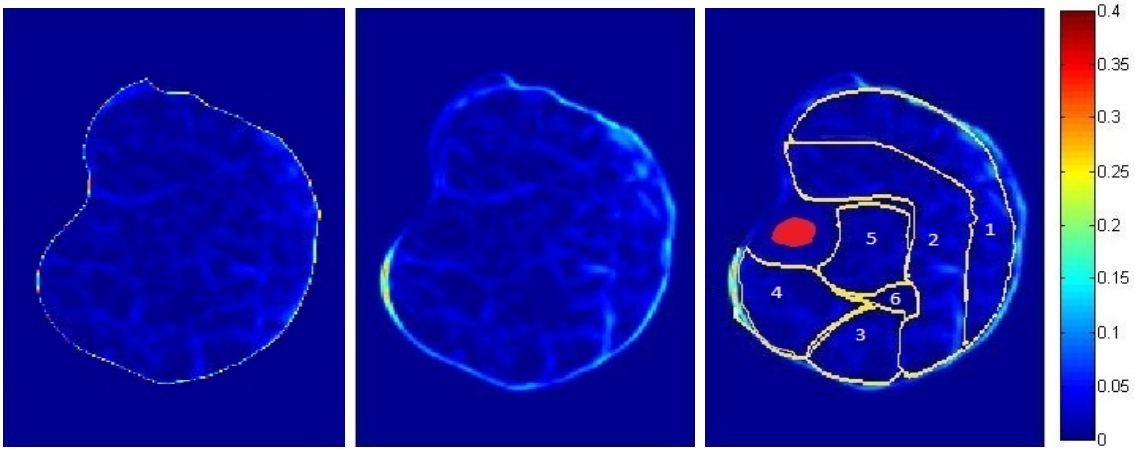

Figure 4.11. 30th slice of Baseline strain maps of Test Subject "C" Left: result from fully elastic registration method Middle: result from our proposed constrained elastic registration method Right: result from our proposed constrained elastic registration with muscle group borders (1:GM,2:SOL,3:PER,4:AC,5:DF,6:fibula) and tibia segmentation mask in red color shown on it.

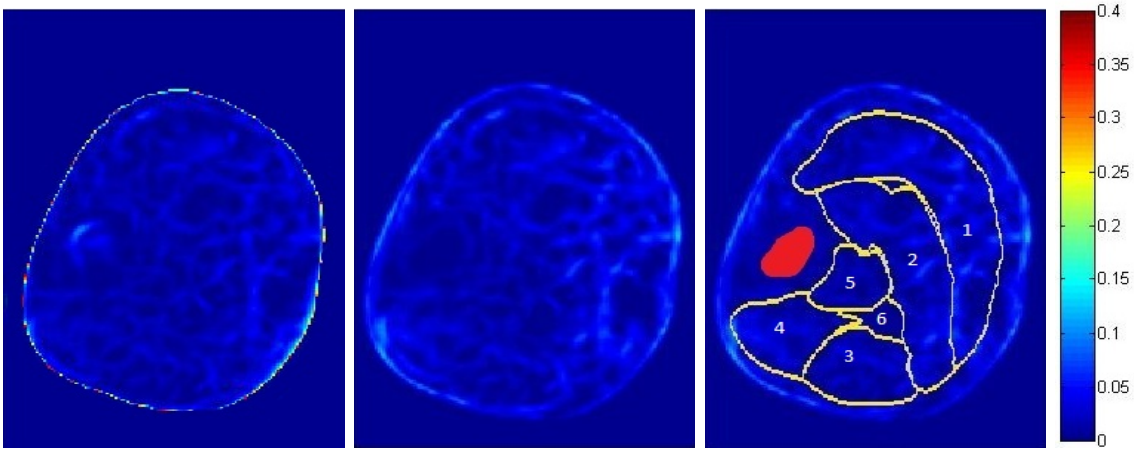

Figure 4.12. 1st slice of Baseline strain maps of Test Subject "D" Left: result from fully elastic registration method Middle: result from our proposed constrained elastic registration method Right: result from our proposed constrained elastic registration with muscle group borders (1:GM,2:SOL,3:PER,4:AC,5:DF,6:fibula) and tibia segmentation mask in red color shown on it.

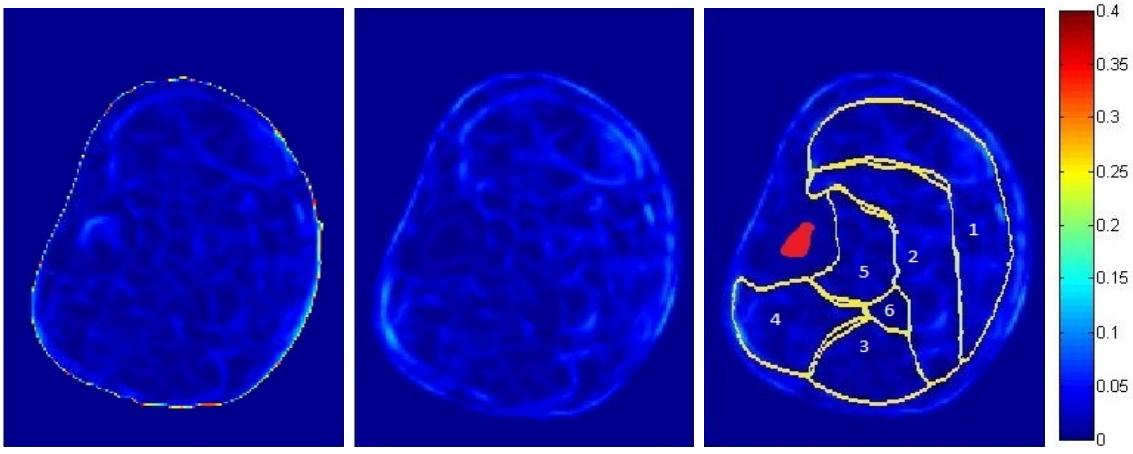

Figure 4.13. 30th slice of Baseline strain maps of Test Subject "D" Left: result from fully elastic registration method Middle: result from our proposed constrained elastic registration method Right: result from our proposed constrained elastic registration with muscle group borders (1:GM,2:SOL,3:PER,4:AC,5:DF,6:fibula) and tibia segmentation mask in red color shown on it.

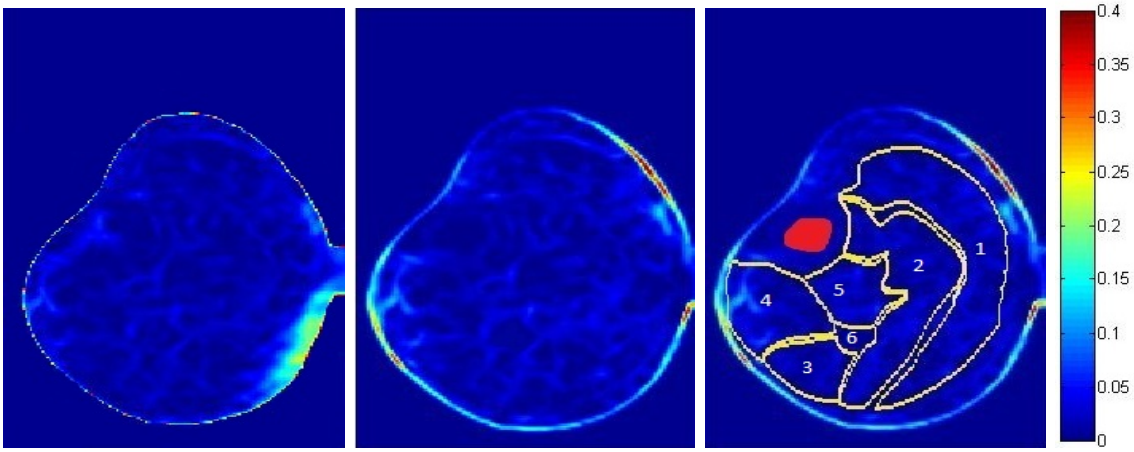

Figure 4.14. 1st slice of Baseline strain maps of Test Subject "E" Left: result from fully elastic registration method middle: result from our proposed constrained elastic registration method Right: result from our proposed constrained elastic registration with muscle group borders (1:GM,2:SOL,3:PER,4:AC,5:DF,6:fibula) and tibia segmentation mask in red color shown on it.

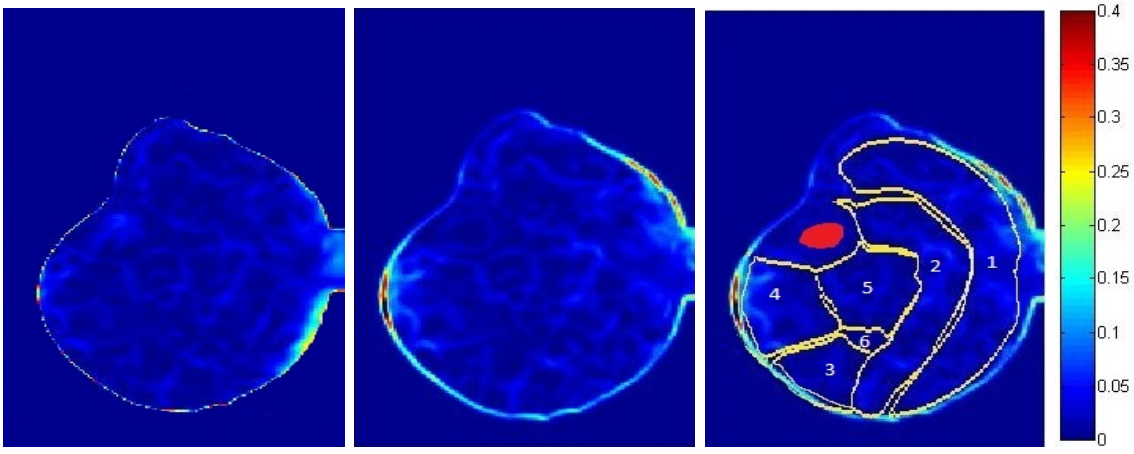

Figure 4.15. 30th slice of Baseline strain maps of Test Subject "E" Left: result from fully elastic registration method Middle: result from our proposed constrained elastic registration method Right: result from our proposed constrained elastic registration with muscle group borders (1:GM,2:SOL,3:PER,4:AC,5:DF,6:fibula) and tibia segmentation mask in red color shown on it.

Table 4.5. Mean ± Standard Deviation Values of Tissue Strains for Unconstrained Elastic Registration Method (R1: complete muscle, R2: muscle boundaries, R3: muscle interior)

Subjects		GM	SOL	DF	PER	AC
A	R1	0.0535±0.0353	0.081±0.0369	0.1004±0.0563	0.051±0.0254	0.0544±0.0264
	R2	0.0609±0.0384	0.1004±0.0465	0.0767±0.0469	0.0468±0.0246	0.0441±0.0196
	R3	0.0529±0.0351	0.0797±0.0359	0.1035±0.0570	0.0514±0.0255	0.0553±0.0268
B	R1	0.0996±0.0687	0.1065±0.0493	0.0773±0.0376	0.1047±0.0502	0.1754±0.1009
	R2	0.0878±0.0556	0.0939±0.0383	0.0759±0.0371	0.0775±0.0493	0.9254±3.3772
	R3	0.1005±0.0697	0.1074±0.0499	0.0775±0.0377	0.1071±0.0496	0.1779±0.0989
C	R1	0.0825±0.0506	0.0526±0.0335	0.0292±0.0355	0.0395±0.0286	0.0603±0.0468
	R2	0.0475±0.0397	0.0479±0.0349	0.0379±0.0360	0.0632±0.0415	0.1016±0.2425
	R3	0.0851±0.0504	0.0529±0.0334	0.0285±0.0353	0.0374±0.0266	0.0605±0.0464
D	R1	0.1025±0.0460	0.0834±0.0376	0.0373±0.0321	0.0447±0.0253	0.0569±0.0374
	R2	0.1090±0.0374	0.0904±0.0390	0.0472±0.0334	0.0445±0.0228	0.0434±0.0251
	R3	0.1021±0.0464	0.0830±0.0374	0.0365±0.0318	0.0447±0.0255	0.0580±0.0381
E	R1	0.1225±0.0690	0.0772±0.0422	0.0650±0.0351	0.0957±0.0355	0.0977±0.0678
	R2	0.1042±0.0683	0.0844±0.0628	0.0818±0.0428	0.0911±0.0245	0.0907±0.0459
	R3	0.1238±0.0688	0.0768±0.0407	0.0639±0.0345	0.0963±0.0366	0.0981±0.0691
Mean±STD	R1	0.0921±0.0258	0.0801±0.0192	0.0618±0.0292	0.0671±0.0306	0.0889±0.0515
	R2	0.0819±0.0479	0.0834±0.0443	0.0639±0.0392	0.0646±0.0325	0.2410±0.7421
	R3	0.0351±0.0541	0.0359±0.0395	0.0570±0.0393	0.0255±0.0327	0.0268±0.0559

Table 4.6. Difference in Mean Values of Tissue Strains Between Regions Away From Borders and Border Regions for Unconstrained Elastic Registration Method

Subjects	**GM**	**SOL**	**DF**	**PER**	**AC**
A	-0.0080	-0.0207	0.0268	0.0046	0.0112
B	0.0127	0.0135	0.0016	0.0296	-0.7475
C	0.0376	0.0050	-0.0094	-0.0258	-0.0411
D	-0.0069	-0.0074	-0.0107	0.0002	0.0146
E	0.0196	-0.0076	-0.0179	0.0052	0.0074
$\overline{Mean}$	0.0110	-0.0034	-0.0019	0.0028	-0.1511

Table 4.7. Mean ± Standard Deviation Values of Tissue Strains for Constrained Elastic Registration Method (R1: complete muscle, R2: muscle boundaries, R3: muscle interior)

Subjects		GM	SOL	DF	PER	AC
A	R1	0.0622±0.0458	0.0754±0.0352	0.0924±0.0510	0.0549±0.0326	0.0648±0.0410
	R2	0.0700±0.0450	0.0920±0.0465	0.0697±0.0440	0.0506±0.0283	0.0461±0.0277
	R3	0.0616±0.0458	0.0743±0.0343	0.0954±0.0514	0.0553±0.0330	0.0664±0.0417
B	R1	0.0929±0.0730	0.0948±0.0493	0.0729±0.0373	0.0980±0.0511	0.1797±0.1571
	R2	0.0712±0.0568	0.0816±0.0360	0.0702±0.0369	0.0721±0.0534	0.1124±0.1047
	R3	0.0945±0.0740	0.0957±0.0501	0.0731±0.0373	0.1003±0.0502	0.1840±0.1589
C	R1	0.0889±0.0558	0.0545±0.0342	0.0331±0.0352	0.0388±0.0293	0.0582±0.0421
	R2	0.0554±0.0446	0.0522±0.0328	0.0412±0.0361	0.0649±0.0425	0.0720±0.1008
	R3	0.0914±0.0558	0.0546±0.0343	0.0324±0.0350	0.0364±0.0271	0.0582±0.0419
D	R1	0.1017±0.0459	0.0818±0.0374	0.0378±0.0299	0.0478±0.0292	0.0556±0.0354
	R2	0.1098±0.0352	0.0880±0.0376	0.0483±0.0327	0.0437±0.0254	0.0458±0.0288
	R3	0.1013±0.0465	0.0814±0.0374	0.0369±0.0296	0.0481±0.0295	0.0564±0.0359
E	R1	0.1222±0.0697	0.0773±0.0421	0.0641±0.0342	0.0866±0.0334	0.0919±0.0618
	R2	0.1033±0.0693	0.0824±0.0626	0.0813±0.0423	0.0797±0.0277	0.0845±0.0436
	R3	0.1234±0.0696	0.0771±0.0408	0.0629±0.0336	0.0873±0.0341	0.0924±0.0628
Mean±STD	R1	0.0936±0.0217	0.0768±0.0146	0.0601±0.0247	0.0652±0.0257	0.0900±0.0522
	R2	0.0819±0.0502	0.0792±0.0431	0.0621±0.0384	0.0622±0.0355	0.0722±0.0611
	R3	0.0944±0.0583	0.0766±0.0394	0.0601±0.0374	0.0655±0.0348	0.0915±0.0682

Table 4.8. Difference in Mean Values of Tissue Strains Between Regions Away From Borders and Border Regions for Constrained Elastic Registration Method

Subjects	**GM**	**SOL**	**DF**	**PER**	**AC**
A	-0.0084	-0.0177	0.0257	0.0047	0.0203
B	0.0233	0.0141	0.0029	0.0282	0.0716
C	0.0360	0.0024	-0.0088	-0.0285	-0.0138
D	-0.0085	-0.0066	-0.0114	0.0044	0.0106
E	0.0201	-0.0053	-0.0184	0.0076	0.0079
$\overline{Mean}$	0.0125	-0.0026	-0.0020	0.0033	0.0193

5. DISCUSSION

We have imposed synthetic rigid body motion to the image sets of the *undeformed state* as described in Chapter 4, which served as one of our input datasets in our registration process for getting baseline strain values, while the other input is original deformed data set. Theoretically, imposing rigid body motion should not cause any strains, and thus we expect to see zero or near zero baseline strain values in the final deformation field. Thus, deviations of baseline strain from zero can be interpreted as a measure of accuracy of the registration. Lower baseline strain values correspond to higher accuracy in registration.

From Table 4.1 and Table 4.3, we see that except for GM region of dataset E, unconstrained elastic registration method gives baseline strain values closer to zero for all other datasets and groups than constrained elastic registration. And all those population mean values of unconstrained elastic registration are more smaller than those of constrained elastic registration. By subtracting the baseline strain values of the proposed constrained elastic registration method with the results of unconstrained elastic registration method gives the Table 5.1.

From these differences, we see that for the complete muscle, the differences are all smaller than the standard deviations of the baseline strain values for both unconstrained and constrained elastic registration.

Table 5.1. Difference of Mean Values of Baseline Strains between Unconstrained and Constrained Elastic Registration Method (R1: complete muscle, R2: muscle boundaries, R3: muscle interior)

Subjects		GM	SOL	DF	PER	AC
A	R1	0.0059	0.0044	0.0013	0.0026	0.0049
	R2	0.0085	0.0038	0.0013	0.0035	0.0044
	R3	0.0056	0.0045	0.0013	0.0025	0.0049
B	R1	0.0071	0.0057	0.0035	0.0033	0.0029
	R2	0.0097	0.0072	0.0054	0.0075	-1.0618
	R3	0.0069	0.0055	0.0034	0.0030	0.0025
C	R1	0.0041	0.0061	0.0016	0.0009	-0.0327
	R2	-0.0337	0.0047	0.0011	0.0022	-1.5773
	R3	0.0040	0.0062	0.0016	0.0008	0.0036
D	R1	0.0075	0.0071	0.0022	0.0024	0.0045
	R2	0.0102	0.0046	0.0013	0.0026	0.0044
	R3	0.0073	0.0072	0.0022	0.0023	0.0045
E	R1	-0.0019	0.0048	0.0035	0.0034	0.0111
	R2	-0.0085	0.0041	0.0034	0.0055	0.0089
	R3	-0.0015	0.0048	0.0034	0.0033	0.0112

Also, the baseline values' differences between unconstrained and constrained elastic registration for muscle boundaries are smaller than the standard deviations of the baseline strain values for both unconstrained elastic and constrained elastic registration for muscle boundaries, except for AC muscle region of test datasets B and C. From Tables 4.1, we see that the AC region of test data sets B and C obtained abnormal values both for mean values and standard deviations.

We can take reference to the baseline strain color maps of data set C, as shown in Figure 4.10. For easiness to our discussion, we show the 30th slice color map of test data set C here again:

Subjects	AC
B	1.1017±4.5299
C	1.6116±6.9853

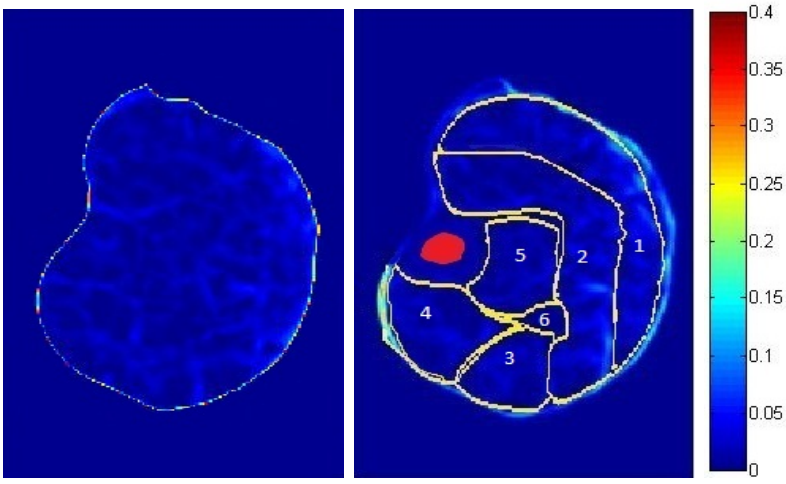

Figure 5.1. 30th slice of Baseline strain maps of Test Subject C
Left: result from unconstrained elastic registration method Right: result from our proposed constrained elastic registration with muscle group borders (1:GM,2:SOL,3:PER,4:AC,5:DF,6:fibula) and tibia segmentation mask in red color shown on it.

This might be due to miscalculation, or incorrect border assignment while obtaining muscle group regions manually. As we see just from these slices, AC regions of these test datasets, which is marked with "4", are somehow closer to the skin regions, and thus while drawing the border lines for AC regions manually, to some degree we might incorrectly included the skin tissues, and hence affected our observation here. But this abnormality is believed not to affect the overall evaluation of the performance.

For the muscle interiors, we also observed the similar result: the differences between baseline strain values of unconstrained and constrained elastic registration are smaller than all the standard deviations of baseline strain values for muscle interiors of unconstrained and constrained elastic registration.

For deducing whether these baseline strain values are affected by muscle borders, we also take reference to the differences of baseline strain values from unconstrained and the proposed constrained elastic registration. From Table 4.2, we see that in unconstrained elastic registration method, except GM regions of test datasets A, B, C and D, together with the AC regions of test data sets B and C which give abnormal values mostly due to miscalculation or incorrect border obtainment, the baseline strain value differences between muscle interior regions and muscle borders are smaller than the standard deviations of both of them for all other muscle regions of all test data sets. For instance, the difference value of DF region for B is "0.0019", and this is smaller than the standard deviation of DF region of data set B for muscle interior regions, which equals "0.0082" in the Table 4.1, and that for muscle borders, which equals "0.0071". As mentioned in Chapter 4, in 'Strain Analysis Results' subsection, it is normal to obtain deformation in GM region according to force transmission mechanism through muscles, but what we concern more about is the remaining SOL, DF, PER and AC regions. Thus, the fact that we obtain closer to zero baseline strain values for GM regions of test data sets A, B, C and D in unconstrained elastic registration does not affect the general evaluation of baseline strain values for muscle interior regions.

Similarly we can see that, from Table 4.4, except AC region of test data set B, all other regions of all datasets give differences of baseline strain values smaller than those standard deviations of both muscle interior regions and muscle borders. For instance, the baseline strain value difference of test dataset C in SOL region is "0.0049", which is smaller than the standard deviation of the same region of data set C for muscle interior regions which equals "0.0149" in the Table 4.3, and that for muscle borders which equals "0.0139".

For the tissue strains, for gastrocnemius (GM) region, we see that data sets B, D and E get bigger strain values in unconstrained elastic registration, while A and C get bigger ones in the proposed constrained elastic registration. The population mean value of the proposed constrained elastic registration is bigger. For muscle interior regions, we find that unconstrained elastic method is giving bigger tissue strain values for datasets B, D and E, while the proposed constrained elastic registration gives bigger

tissue strain values for data sets A and C, as shown in the Table 4.5. For muscle borders, datasets B and E get bigger tissue strains in unconstrained elastic registration while datasets A, C and E get bigger strains in the proposed constrained elastic registration, as shown in the Tables 4.5, and 4.7. Thus, except dataset D, for muscle border regions we get the same result in accordance with those of muscle interior regions and the population mean of tissue strain values.

For soleus (SOL) region, datasets A, B and D get bigger tissue strain values in unconstrained elastic registration method, while datasets C and E give bigger values in the proposed constrained elastic registration. The population mean value of tissue strains is bigger in unconstrained elastic registration method, as shown in tables 4.5 and 4.7. For muscle interior regions, we see that unconstrained elastic registration method gives bigger strain values for datasets A, B and D. For muscle borders, unconstrained elastic registration gets bigger strain values for datasets A, B, D, E and bigger population mean.

For deep flexors (DF) region, datasets A, B and E get bigger tissue strain values in unconstrained elastic registration method, which also gives bigger population mean tissue strain value. For muscle interior regions, we see that datasets A, B, and E get bigger strain values in unconstrained elastic registration, as shown in tables 4.5 and 4.7. For muscle borders, datasets A, B and E get bigger tissue strain values in unconstrained elastic registration method, which also gives bigger population mean value.

For peronei muscle group (PER), datasets B, C and E give bigger tissue strain values in unconstrained elastic registration method, which also gives bigger population mean of tissue strain value. For muscle interior regions, we can see that datasets B, C and E get bigger tissue strain values in unconstrained elastic registration while the proposed constrained elastic registration gets bigger values for datasets A and D, as well as bigger population mean of tissue strain values, as shown in Tables 4.5 and 4.7. For muscle borders, datasets B, D and E get bigger tissue strain values in unconstrained elastic registration, which also gives bigger population mean value.

For anterior crural (AC) muscle group, datasets C, D and E get bigger tissue strain values in unconstrained elastic registration method, while datasets A and B get bigger tissue strain values in the proposed constrained elastic registration, which also gives bigger population mean value. For muscle interior regions, datasets C, D and E give get bigger tissue strain values in unconstrained elastic registration method. For muscle borders, datasets B, C, and E get bigger strain values in unconstrained elastic registration, which also gives bigger population mean value.

From Table 4.6, we see that only except for AC group of dataset B, all other groups of data sets give mean differences that are smaller than both of the standard deviations of muscle borders and muscle interior regions. As we discussed in the baseline strain part before, there could be a potential miscalculation or incorrect manual subtraction of the muscle group border for this AC group of test dataset B.

From Table 4.8, we see that all the five muscle groups of all five test data sets give mean differences that are smaller than both of the standard deviations of muscle borders and muscle interior regions.

Thus, from the aspect of tissue strains, unconstrained elastic registration gives bigger strain values for our data sets than the proposed constrained elastic registration method.

Intuitively, the proposed constrained elastic registration method gives higher accuracy than unconstrained registration method. Not fixing the fibula is a drawback of the algorithm, but to compensate for this, the fibula region's deformation is initialized through a rigid registration as presented in Chapter 3. As we see, the differences between strain values of muscle border regions and internal muscles in both unconstrained and the proposed constrained elastic registration are smaller than their standard deviations, by which we deduce that both the unconstrained and the proposed constrained elastic registration methods are applicable to estimate deformation among muscles. Yet, the proposed constrained elastic registration method holds more accuracy by construction.

6. CONCLUSION

In this work, we proposed a constrained elastic registration method for MR images of human lower leg to obtain a deformation field for strain calculations, which is important for observing force transmission across and along muscles. In classical methods, the deformation fields are obtained by elastically registering the MR images, including bone regions. However, bone tissue is hard compared to muscle, so the deformation values for bone regions, which is further used for strain analysis, are inaccurate. The contribution of the proposed method is that the bone regions are no longer registered elastically, instead they are fixed, leading to accurate final deformation field and strain analysis in bones. We performed tibia and fibula segmentation from the given data, rigidly aligned the tibia and built an initial deformation field using the fibula regions. They are used to perform the constrained elastic registration. We then calculated strain values from the final deformation field obtained by the proposed method and compared it with that of the unconstrained elastic registration method.

We manually divided the lower leg region into five different muscle groups, and calculated the baseline and tissue strain values for them separately.We applied synthetic rigid motion to the original undeformed state data set to manually obtain deformed state data set, and used it with the original deformed data set for the registration framework. Smaller absolute baseline strain values are interpreted as better accuracy in deformation field computation. We expected to see our proposed constrained elastic registration to have baseline strain values closer to zero. We carried out strain analysis for each of the five different muscle groups. In order to assess the affect of muscle boundaries, we also performed the same calculation for the border and internal muscle regions separately. We observed that the unconstrained elastic registration method results in closer to zero baseline strain values than the constrained elastic registration method for both boundary and internal muscle regions. The results indicate that the muscle borders and the muscle interior regions are not significantly different for the unconstrained and the proposed constrained elastic registration methods. However, the difference is small compared to the intrapatient deviation of the strain values, sug-

gesting that both approaches are viable to estimate deformation inside the muscles. Yet, the proposed constrained elastic registration method provides more accurate results in the bones by construction. However, a primary limitation of this work is the small dataset used. Further experiments with a larger dataset and variable experiment protocols are required to reach more reliable conclusion. The topic of image based deformation analysis remains to be investigated further.

REFERENCES

1. Yucesoy, C. A., *IntraIntra-, Inter- and Extramuscular Myofascial Force Transmission: A Combined Finite Element Modeling and Experimental Approach*, DPP-Utrech B.V., Utrech, The Netherlands, 2003.

2. Yucesoy, C. A., G. C. Baan and P. A. Huijing, "Epimuscular Myofascial Force Transmission Occurs in the Rat Between the Deep Flexor Muscles and Their Antagonistic Muscles", *Journal of Electromyography and Kinesiology*, Vol. 20, pp. 118–126, 2010.

3. Yucesoy, C. A., G. C. Baan, B. H. Koopman, H. J. Grootenboer and P. A. Huijing, "Pre-strained Epimuscular Connections Cause Muscular Myofascial Force Transmission to Affect Properties of Synergistic EHL and EDL Muscles of the Rat", *Journal of Biomechanical Engineering*, Vol. 127, No.5, pp. 819–828, 2005.

4. Yucesoy, C. A., G. C. Baan and P. A. Huijing, "Substantial Effects of Epimuscular Myofascial Force Transmission on Muscular Mechanics Have Major Implications on Spastic Muscle and Remedial Surgery", *Journal of Electromyography and Kinesiology*, Vol. 17, pp. 664–679, 2007.

5. Huijing, P. A., A. Yaman, C. Ozturk and C. A. Yucesoy, "Effects of Knee Joint Angle on Global and Local Strains Within Human Triceps Surae Muscle: MRI Analysis Indicating *In Vivo* Myofascial Force Transmission Between Synergistic Muscles", *Surgical and Radiologic Anatomy*, Vol. 33, pp. 869–879, 2011.

6. Steger, S. and S. Wesarg, "Automated Skeleton Based Multi-modal Deformable Registration of Head&Neck Datasets", *Medical Image Computing and Computer-Assissted Intervention*, pp. 66–73, 2012.

7. Peterfy, C. G., G. Gold, F. Eckstein, F. Cicuttini, B. Dardzinski and R. Stevens, "MRI Protocols for Whole-organ Assessment of the Knee in Osteoarthritis", *Os-*

teoarthritis and Cartilage, Vol. 14, Supplement 1, pp. 95–111, 2006.

8. Kratky, J. and J. Kybic, "Three-dimensional Segmentation of Bones From CT and MRI Using Fast Level Sets", *Medical Imaging 2008: Image Processing*, Vol. 6914, pp. 47–50, 2008.

9. Schmid, J., J. Kim and N. Magnenat-Thalmann, "Robust Statistical Shape Models for MRI Bone Segmentation in Presence of Small Field of View", *Medical Image Analysis 15 (2011)*, pp. 155–168.

10. Dodin, P., J. Martel-Pelletier, J.-P. Pelletier and F. Abram, "A Fully Automated Human Knee 3D MRI Bone Segmentation Using the Ray Casting Technique", *Medical, Biological Engineering and Computing*, pp. 1413–1424, 2011, Dec.

11. Lrigo, L. M., O. Faugeras, W. E. L. Grimson, R. Keriven and R. Kikinis, "Segmentation of Bone in Clinical Knee MRI Using Texture-Based Geodesic Active Contour", *Medical Image Computing and Computer-Assisted Intervention*, 1998.

12. Koch, M., A. G. Schwing, D. Comaniciu and M. Pollefeys, "Fully Automatic Segmentation of Wrist Bones For Arthritis Patiens", *ISBI 2011*, pp. 636–640.

13. Shan, L., C. Zach, M. Styner, C. Charles and M. Niethammer, "Automatic Bone Segmentation and Alignment From MR Knee Images", *ISBI' 10 Proceedings of the 2010 IEEE International Conference on Biomedical Imaging: From Nano to Macro*.

14. Shan, L., C. Zach and M. Niethammer, "Automatic Three-lable Bone Segmentation From Knee MR Images", *2010 IEEE International Symposium on Biomedical Imaging: From Nano to Macro*.

15. Schmid, J. and N. Magnenat-Thalmann, "MRI Bone Segmentation Using Deformable Models and Shape Priors", *Medical Image Computing and Computer-Assisted Intervention - MICCAI*, pp. 119–126, 2008.

16. Liu, J., J. k. Udupa, P. k. Saha, D. Odhner, B. E. Hirsch, S. Seigler, S. Simon and B. A. Winkelstein, "Rigid Model-based 3D Segmentation of the Bones of Joints in MR and CT Images for Motion Analysis", *Departmental Papers, Department of Bioengineering, University of Pennsylvania*, 2008.

17. Zhang, J., C. H. Yan, C. K. Chuil and S. H. Ong, "Fast Segmentation of Bone in CT Images Using 3D Adaptive Thresholding", *Computers in Biology and Medicine*, pp. 231–236, 2010.

18. Rifai, H., I. Bloch, S. hutchinson, J. Wiart and L. Garnero, "Segmentation of the Skull in MRI Volumes Using Deformable Model and Taking the Partial Volume Effect Into Account", *Medical Image Analysis*, pp. 219–233, 2000, Sep.

19. Thevenaz, P. and M. Unser, "Optimization of Mutual Information for Multiresolution Image Registration", *IEEE Transactions on Image Processing*, Vol. 9 No.12, December 2000.

20. Klein, S., M. Staring, K. Murphy, M. A. Viergever and J. P. W. Pluim, "elastix: A Toolbox for Intensity-Based Medical Image Registration", *IEEE Transactions on Medical Imaging*, Vol. 29 No.1, January 2010.

21. Thirion, J. P., "Image Matching as a Diffusion Process: an Analogy with Maxwell's Demons", *Medical Image Analysis*, pp. 243–260, 1998.

22. Thirion, J. P., "Fast Non-Rigid Matching of 3D Medical Image", *technical Report, Research Report RR-2547, Epidure Project, INRIA Sophia*, May 1995.

23. "Isolated Connected Component Image Filter", *National Library of Medicine*, http://www.itk.org/Doxygen/html/classitk/IsolatedConnectedImageFilter.html, 2009.

24. Klein, S., M. Staring, K. Murphy, M. A. Viergever and J. Pluim, "elastix: A Toolbox for Intensity-Based Medical Image Registration", *IEEE Transactions on*

Medical Imaging, 2010.

25. Ibanez, L., *The ITk Software Guide: Insight Segmentation and Registration Toolkit*, http://www.itk.org/UserGuide, 2009.

26. *Insight Segmentation and Registration Toolkit (ITK)*, National Library of Medicine, `http://www.itk.org/, 2009`.

27. Yaman, A., C. Ozturk, P. A. Huijing and C. A. Yucesoy, "MRI Assessment of Mechanical Interactions Between Human Lower Leg Muscles in vivo", *Journal of Biomechanical Engineering*.